Impact of a new anisotropic rheology on simulations of Arctic sea ice

M. Tsamados,[1,2] D. L. Feltham,[1,2] and A. V. Wilchinsky[1,2]

Received 17 February 2012; revised 24 September 2012; accepted 8 November 2012.

[1] A new rheology that explicitly accounts for the subcontinuum anisotropy of the sea ice cover is implemented into the Los Alamos sea ice model. This is in contrast to all models of sea ice included in global circulation models that use an isotropic rheology. The model contains one new prognostic variable, the local structure tensor, which quantifies the degree of anisotropy of the sea ice, and two parameters that set the time scale of the evolution of this tensor. The anisotropic rheology provides a subcontinuum description of the mechanical behavior of sea ice and accounts for a continuum scale stress with large shear to compression ratio and tensile stress component. Results over the Arctic of a stand-alone version of the model are presented and anisotropic model sensitivity runs are compared with a reference elasto-visco-plastic simulation. Under realistic forcing sea ice quickly becomes highly anisotropic over large length scales, as is observed from satellite imagery. The influence of the new rheology on the state and dynamics of the sea ice cover is discussed. Our reference anisotropic run reveals that the new rheology leads to a substantial change of the spatial distribution of ice thickness and ice drift relative to the reference standard visco-plastic isotropic run, with ice thickness regionally increased by more than 1 m, and ice speed reduced by up to 50%.

Citation: Tsamados, M., D. L. Feltham, and A. V. Wilchinsky (2013), Impact of a new anisotropic rheology on simulations of Arctic sea ice, *J. Geophys. Res. Oceans*, *118*, doi:10.1029/2012JC007990.

1. Introduction

[2] The rapid decrease of the Arctic sea ice extent and volume over recent years raises questions as to the importance of this decline both in the global climatic system and at the regional scale. An important contribution to our understanding of this changing region of the world lies in the correct description of the rheological and mechanical properties of the Arctic ice cover. Although the determination of suitable constitutive relations to describe sea ice rheology remains an outstanding problem that limits the success of sea ice models [*Pritchard*, 2001; *Feltham*, 2008], the climate modeling community has converged, as evidenced by the latest International Panel on Climate Change Fourth Assessment Report, to the almost exclusive use of a rheology of the viscous-plastic type (VP) [*Hibler III*, 1979] based upon the earlier AIDJEX model [*Coon et al*., 1974]. A commonly used example of a VP rheology is the elastic-visco-plastic (EVP) rheology that is used in the Los Alamos sea ice model (CICE) [*Hunke and Lipscomb*, 2008]. *Kreyscher et al*., [2000] showed that this type of rheology performs better in reproducing the spatial pattern and average thickness of sea ice as well as the regional ice drift and Fram strait outflow, than other, more crude, descriptions of the rheology where the ice pack is in free drift, behaves as a compressible viscous Newtonian fluid, or has no shear strength.

[3] Nevertheless, important differences between the results from models using a VP rheology and observations remain. Comparison with ice thickness obtained from submarine cruises have shown simulated ice that is too thick in the Beaufort sea and too thin near the North Pole [*Miller et al*., 2005; *Kreyscher et al*., 2000]. Detailed analysis of ice motion using the RADARSAT Geophysical Processor System [*Kwok et al*., 2008] shows that models underestimate ice drift off the coast of Alaska and Siberia, poorly reproduce time series of shear, vorticity and particularly divergence at the regional scales, and consistently underestimate deformation-related ice volume production. *Rampal et al*. [2011] argues that this deficiency of the current International Panel on Climate Change climate models to accurately capture the coupling between the ice state and dynamics could partly explain the models' underestimation of the recent sea ice area, thickness, and velocity trends.

[4] The discrepancies between models and observations suggest that one needs to question the underlying assumptions used in the development of the VP models [e.g., *Coon et al*., 2007]. First, with new computer capabilities, sea ice models can be routinely run at length scales of 10 km or less, but because sea ice is composed of polygonal floes (Figure 1) of sizes ranging from tens of meters to tens of kilometers, this raises the question of the validity of a continuum description of sea ice at these scales. The issue of the validity of the continuum assumption, closely tied to the scale dependence of the rheology, is discussed in *Feltham* [2008] (Appendix C). Discrete element approaches, which resolve

[1]National Centre for Earth Observation: Centre for Polar Observation and Modelling, University College London, London.

[2]National Centre for Earth Observation: Centre for Polar Observation and Modelling, Department of Meteorology, University of Reading, Reading, UK.

Corresponding author: M. Tsamados, Centre for Polar Observation and Modelling, Department of Meteorology, University of Reading, PO Box 243, Reading RG6 6BB, UK. (m.c.tsamados@reading.ac.uk)

2169-9275/13/2012JC007990

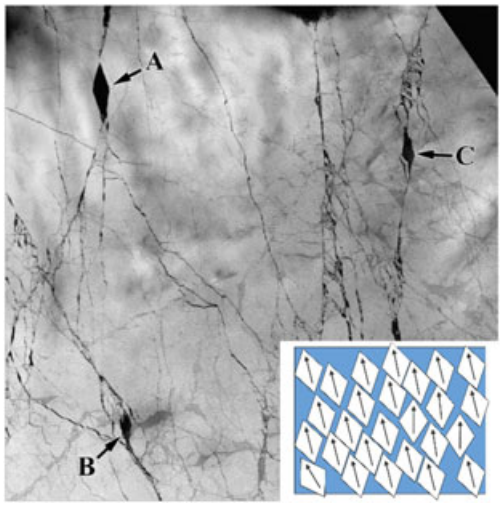

Figure 1. LANDSAT-7 image taken on 25 March 2000, centered around 80°0′N, 135°42′W showing various fractures and faults. The features labeled A, B, and C are evidence of wing cracks. (Taken from *Weiss and Schulson* [2009]). Inset: schematic of diamond shaped floes.

individual floes, have been used to study sea ice dynamics but remain computationally unsuitable for climate simulation [e.g., *Hopkins et al*., 2004; *Wilchinsky et al*., 2011].

[5] Second, in contrast with in situ data obtained during the Surface HEat Budget of the Arctic (SHEBA) and Sea Ice Mechanics Initiative (SIMI) experiments [*Coon et al*., 1998; *Weiss et al*., 2007], early versions of the VP rheology did not account for the capacity of sea ice to withstand tension. *Hibler III* [1979] showed that doubling the shear strength in an isotropic model reduced the flow over the Arctic Basin, causing a reduction of outflow and ice drift and an increase of the average ice thickness by about 5%. More recently *Zhang and Rothrock* [2005], *Miller et al*. [2005] and *Wilchinsky et al*. [2006] showed that by modifying the shape of the yield curve, for example by increasing the shear strength or by incorporating biaxial tensile stress, a better agreement with observed ice thickness distribution could be achieved.

[6] Third, most currently used models of sea ice do not treat explicitly the sea ice elasticity. Yet *Wilchinsky et al*. [2010, 2011] and *Girard et al*. [2011] have recently shown that accounting for elasticity, in particular through the long range interactions that it allows in the ice cover, enables models to more accurately reproduce the degree of localization of the sea ice deformation.

[7] Finally, and more crucially for this article, the hypothesis of isotropy was shown to be inaccurate at the resolution at which most models are run today. Figure 1, a 50×50 km^2 optical image from the LANDSAT-7 satellite [*Weiss and Schulson*, 2009], shows a typical sea ice area composed of various fractures and faults. In this area of sea ice, which coincides with the typical grid size used in sea ice models, a network of intersecting leads imparts to the sea ice cover a preferred orientation with floes of roughly diamond geometry, aligned vertically along the figure. The effect of anisotropy has been treated either explicitly through consideration of particular leads [*Coon et al*., 1998; *Pritchard*, 1998; *Hibler III and Schulson*, 2000; *Hibler III*, 2001; *Schreyer et al*., 2006; *Wilchinsky et al*., 2011] or implicitly through continuum representation of anisotropy using heuristic arguments [*Wilchinsky and Feltham*, 2004a, 2006b]. Additionally, *Wilchinsky and Feltham* [2006a], motivated by satellite imagery, treated the ice cover as comprising diamond-shaped ice blocks formed from intersecting slip lines, to develop an anisotropic sea ice model avoiding detailed modeling of fracture processes. In this paper, we do not resort to the assumption of isotropy and implement into the Los Alamos CICE sea ice model a new rheology [*Wilchinsky and Feltham*, 2006a] that explicitly accounts for the subgrid scale anisotropy of the sea ice cover. We use this model to perform the first continuum Arctic Basin scale simulation of sea ice that explicitly accounts for the subcontinuum anisotropy of the sea ice cover.

[8] The paper is structured as follows: In section 2 we introduce the anisotropic model and discuss issues relevant to its implementation in the Los Alamos CICE sea ice model. In section 3 we apply our model to the Arctic Ocean using realistic forcing. We compare our anisotropic sea ice model simulations to those obtained with the standard, isotropic sea ice model and discuss how the introduction of anisotropy changes the simulated sea ice mechanical behavior. We then proceed, in section 4, to a sensitivity study demonstrating the impact of the new anisotropic model parameters. Finally, in section 5 we summarize our main results and discuss some implications of our work.

2. The Anisotropic Model

2.1. The Sea Ice Stress

[9] To determine the stress arising in sea ice motion, *Wilchinsky and Feltham* [2006a] (WF) considered a simple kinematic model of relative ice floe movement proposed by Ukita and Moritz (UM) [*Ukita and Moritz*, 1994, 2000; *Moritz and Ukita*, 2000]. This model related the relative motion of adjacent sea ice floes to the large-scale rate of deformation of the sea ice cover. UM calculated explicitly the ridging and sliding functions (see section 2.3) and derived the associated plastic yield curve by applying minimization of the maximum shear stress, σ_{II}, to a linear combination of the estimated ridging and sliding coefficients. This minimization approach generates an isotropic rheology with alignment of the principal directions of the stress and strain rate tensors. *Wilchinsky et al*. [2006] used this method to compute the yield curve associated with a random isotropic geometry of floes and applied it in Arctic Basin scale simulations, showing that this isotropic model performed better in reproducing the thickness and drift of the sea ice than isotropic VP models that use the standard elliptic yield curve. *Taylor et al*. [2006] took a somewhat different approach: they calculated relative floe motion using the kinematic model of UM but calculated sea ice stress from a consideration of the deformation of the ice in the leads separating the floes and using the mean stress theorem to calculate the large-scale sea ice stress from the integral of edge tractions. This approach allowed an investigation of the scale-dependence of sea ice rheology and the (restrictive) conditions under which the ice cover could be considered isotropic.

[10] *Wilchinsky and Feltham* [2006a] generalized the *Taylor et al*. [2006] approach to calculate the anisotropic sea ice stress associated with an idealized sea ice cover

consisting of closely interlocking, diamond-shaped ice floes delineated by slip lines. This underlying anisotropic tiling of the sea ice cover is supported by observations (Figure 1) and was also shown to emerge through discrete element simulations of the sea ice [*Wilchinsky et al*., 2011]. As described in greater detail in *Wilchinsky and Feltham* [2006a], WF calculated directly the internal stress for a single orientation of the ice floes, defined by the unit vector **r** along the floe main diagonal (Figure 2), and for an average ice thickness h, and decomposed it into its ridging (r) and sliding (s) contributions

$$\sigma^b(\mathbf{r},h) = P_r(h)\sigma_r^b(\mathbf{r}) + P_s(h)\sigma_s^b(\mathbf{r}), \tag{1}$$

with

$$\sigma_r^b(\mathbf{r}) = \Big[\frac{-1}{sin2\phi}[H(-\dot{\varepsilon}:\mathbf{n}_1\tau_2)\mathbf{n}_1\tau_2 + H(-\dot{\varepsilon}:\mathbf{n}_2\tau_1)\mathbf{n}_2\tau_1\Big]_{sym},$$
$$\sigma_s^b(\mathbf{r}) = \Big[\frac{1}{sin2\phi}sgn(\dot{\varepsilon}:\tau_2\tau_1)[H(-\dot{\varepsilon}:\mathbf{n}_1\tau_2)\tau_1\tau_2 + H(-\dot{\varepsilon}:\mathbf{n}_2\tau_1)\tau_2\tau_1]\Big]_{sym}, \tag{2}$$

where P_r and P_s are the ridging and sliding strengths, $\dot{\varepsilon} = \{\dot{\varepsilon}_{ij}\}$ is the large-scale strain rate tensor, and the various geometrical terms appearing in these two equations are defined in Figure 2. Here we have assumed that the opening strength is sufficiently small to justify the omission of an opening contribution in equation 1. ϕ is half of the acute angle of the diamonds, the relative velocity between the two floes connected by the vector $L\tau_2$ is $\mathbf{v} = L\tau_2\cdot\dot{\varepsilon}$, where the large-scale vorticity is neglected [*Moritz and Ukita*, 2000], the Heaviside terms, $H(\cdot)$, are used to activate the ridging and sliding forces when adjacent floes are approaching each other, and the suffix "sym" denotes the symmetric part, i.e., $\mathbf{X}_{\mathrm{sym}} = \frac{1}{2}\left(\mathbf{X} + \mathbf{X}^T\right)$, where "T" denotes the transpose. In equation 2 we used only the symmetric part of the stress tensors to satisfy the no spin assumption. In determining this stress expression WF considered parallel floes, but in a continuum-scale sea ice region (with a lateral scale of, say, 100 km) the floes can possess different orientations in different places (Figure 1). Because observations show that ice floe orientation varies gradually, we neglect any stress that can arise through interactions between nonaligned ice floes. In this case, if floe orientation is given by a probability density function $\psi(\mathbf{r}) = \psi(-\mathbf{r})$, then the mean sea ice stress over a collection of floes is given by the average

$$\sigma(h) = P_r(h)\int_{\mathbb{S}}\psi(\mathbf{r})\left[\sigma_r^b(\mathbf{r}) + k\sigma_s^b(\mathbf{r})\right]d\mathbf{r}, \tag{3}$$

where $\mathbb{S}$ is a unit-radius circle and we introduce the friction parameter $k = P_s/P_r$. As discussed in WF, k has only a weak dependence on ice thickness and has been experimentally shown to take values in the range 0.4 to 2. In this paper we will therefore use k as a constant free parameter. In expression 3 the stress tensor dependence on the local anisotropy of the underlying diamond-shaped structure of the sea ice cover is quantified by the probability density function $\psi(\mathbf{r})$. A theory that considers the full probability density function is somewhat complicated [*Wilchinsky and Feltham*, 2012] and we consider a more practical approach here. For simplicity we take $\psi(\mathbf{r})$ to be Gaussian, $\psi(z) = \omega_1 \exp(-\omega_2 z^2)$, where z is the ice floe inclination with respect to the axis x_1 of preferential alignment of ice floes (see Figure 2), $\psi(z)$ is periodic with period π, and the positive coefficients ω_1 and ω_2 are calculated to ensure normalization of $\psi(z)$, i.e., $\int_0^{2\pi}\psi(z)dz = 1$, and the ratio of the principal components of $\mathbf{A}$, A_1/A_2, derived from below (equation 5). We define the structure tensor

$$\mathbf{A} = \int_{\mathbb{S}}\psi(\mathbf{r})\mathbf{r}\mathbf{r}d\mathbf{r}. \tag{4}$$

[11] From now on we shall describe the orientational distribution of floes using the structure tensor. Specifically the degree of anisotropy is measured by the largest eigenvalue (A_1) of this tensor ($A_2 = 1 - A_1$). $A_1 = 1$ corresponds to perfectly aligned floes and $A_1 = 0.5$ to a uniform distribution of floe orientation. Note that while we have specified the aspect ratio of the diamond floes, through prescribing ϕ, we make no assumption about the size of the diamonds so that formally the theory is scale invariant. Finally, note that in this paper we use for the ridging ice strength, $P_r(h)$ in equation 3, the formulation of *Rothrock* [1975] where the strength is assumed to be proportional to the change in ice potential energy per unit area of compressive deformation. The values of the parameters used in this strength formulation are taken from *Lipscomb et al*. [2007] and *Hunke and Lipscomb* [2008]. We see that with equations 2 to 4 we have presented a general expression for the internal stress tensor of sea ice that explicitly accounts for the subcontinuum anisotropy of the ice through the probability distribution function ψ calculated from local structure tensor **A**. For more details on the computation of the anisotropic stress tensor in CICE we refer the reader to section 2.4 and to section A1.

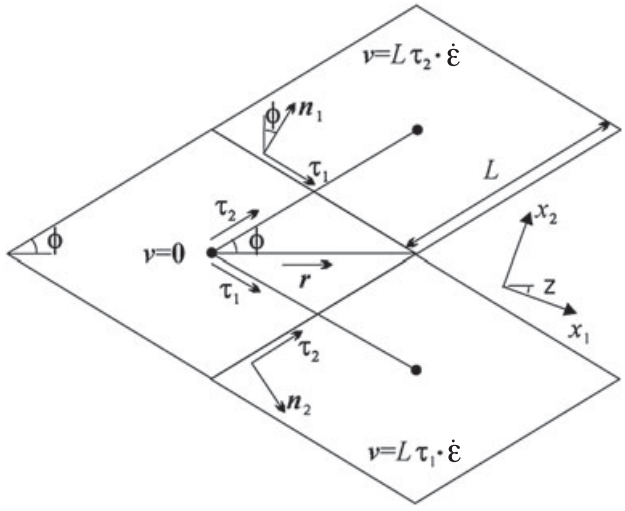

Figure 2. Geometry of interlocking diamond-shaped floes. (Taken from *Wilchinsky and Feltham* [2006a]). ϕ is half of the acute angle of the diamonds. L is the edge length. $\mathbf{n}_1$, $\mathbf{n}_2$ and τ_1, τ_2 are respectively the normal and tangential unit vectors along the diamond edges. $\mathbf{v} = L\tau_2\cdot\dot{\varepsilon}$ is the relative velocity between the two floes connected by the vector $L\tau_2$. **r** is the unit vector along the main diagonal of the diamond. Note that the diamonds illustrated here represent one possible realization of all possible orientations. The angle z represents the rotation of the diamonds' main axis relative to their preferential orientation along the axis x_1.

2.2. Evolution of Ice Floe Orientation

[12] We now need to describe how the local degree of anisotropy quantified by the structure tensor **A** evolves in time. In the deforming Arctic the ice floes can change their orientation through rigid body rotation determined by the vorticity tensor but also following the ensemble continuum-scale deformation determined by the strain rate tensor. Other processes, however, tend to change the floe shapes and therefore affect the degree of anisotropy of the pack ice: fracture of the sea ice cover can generate new intersecting slip lines delineating ice floes of another orientation, which will alter the shape of the existing floes; freezing and melting at the floe edges can lead to a change of the floe shape; and several ice floes can freeze together to form an ice floe of a new, arbitrary shape. Fully accounting for the processes that alter floe shape would complicate a model of stress and floe evolution considerably, and the resulting model would be of little use in climate simulations. Following WF, we describe these floe orientation changes with a phenomenological evolution equation for the structure tensor **A**,

$$\frac{D\mathbf{A}}{Dt} = \mathbf{F}_{\mathrm{mech}}(\mathbf{A}, \dot{\varepsilon}) + \mathbf{F}_{\mathrm{iso}}(\mathbf{A}) + \mathbf{F}_{\mathrm{frac}}(\mathbf{A}, \sigma), \tag{5}$$

where t is the time, D/Dt is the corotational time derivative accounting for advection and rigid body rotation ($D\mathbf{A}/Dt = \mathrm{d}\mathbf{A}/\mathrm{d}t - \mathbf{W}\cdot\mathbf{A} - \mathbf{A}\cdot\mathbf{W}^{\mathrm{T}}$) with $\mathbf{W}$ being the vorticity tensor. $\mathbf{F}_{\mathrm{mech}}$ is a function determining the rotation of the ice floes subjected to the large-scale strain rate. Because the strain rate increases with decreasing length scales, F_{mech} might become important for very-high resolution calculations [*Marsan et al.*, 2004]. In realistic sea ice conditions and for standard global circulation models where the resolution is larger than a few kilometers the strain rate is of the order of 10^{-6} s^{-1} and $\mathbf{F}_{\mathrm{mech}}$ can be neglected since the rates of floe reorientation are of the order of 10^{-4} s^{-1} as confirmed by inspection of sequences of SAR images from RADARSAT, such as those provided by R. Kwok, Jet Propulsion Laboratory, available at www-radar.jpl.nasa.gov/rgps/image_files/combine_small.gif.

[13] $\mathbf{F}_{\mathrm{iso}}$ is a function that accounts for a variety of processes that contribute to convey a more isotropic nature to the ice cover. When ice fractures without formation of an open lead the newly formed ice blocks can consolidate at least partly to reconstruct the original block. On the other hand even when an open lead is formed it becomes a region that is prone to ridge formation through collision of separated floes and ice tends to return to a more isotropic structure. It is also well established [*Weiss et al.*, 2007] that thermally-induced tensile stresses can induce thermal cracking that can result again in a more isotropic ice cover. Finally, in the summer, melting breaks the densely packed ice into a cover that resembles an isotropic granular medium. Therefore all these mechanisms lead to an isotropic distribution of floe orientation and this process is parametrized in a simplified manner by

$$\mathbf{F}_{\mathrm{iso}} = -k_i\left(\mathbf{A} - \frac{1}{2}1\right), \tag{6}$$

where k_{i} is the rate of relaxation toward an isotropic sea ice cover. This is a poorly constrained parameter and we take a reference value of $k_i = 2\cdot 10^{-4}\mathrm{s}^{-1}$ corresponding to a thermodynamic time scale of 5000 s.

[14] Finally, the last term on the right-hand side of equation 5, $\mathbf{F}_{\mathrm{frac}}$, is a function determining the ice floe reorientation due to fracture, and explicitly depends upon sea ice stress (but not its magnitude). Following WF, four failure mechanisms, observed in laboratory experiments under controlled conditions and determined by the ratio of the principal values of the sea ice stress σ_1 and σ_2, are here assumed to remain valid for the Arctic sea ice cover [*Schulson*, 2001]: (i) Under biaxial tension, fractures form across the perpendicular principal axes and therefore counteract any apparent redistribution of the floe orientation; (ii) If only one of the principal stresses is compressive, failure occurs through axial splitting along the compression direction; (iii) Under biaxial compression with a low confinement ratio, ($\sigma_1/\sigma_2 < R$), sea ice fails Coulombically through formation of slip lines delineating new ice floes oriented along the largest compressive stress; (iv) Finally, under biaxial compression with a large confinement ratio, ($\sigma_1/\sigma_2 \geq R$), the ice is expected to fail along both principal directions so that the cumulative directional effect balances to zero. The formulation for $\mathbf{F}_{\mathrm{frac}}$ is

$$\mathbf{F}_{\mathrm{frac}} = \begin{cases} 0 & \text{if } \sigma_1 \geq \sigma_2 > 0, & \text{case } (i) \\ -k_f(\mathbf{A}-\mathbf{S}) & \text{if } \sigma_2 < 0 \ \&\ \sigma_1 \geq 0, & \text{case (ii)} \\ -k_f(\mathbf{A}-\mathbf{S}) & \text{if } \sigma_2 \leq \sigma_1 < 0 \ \&\ \sigma_1/\sigma_2 < R, & \text{case (iii)} \\ 0 & \text{if } \sigma_2 \leq \sigma_1 < 0 \ \&\ \sigma_1/\sigma_2 \geq R, & \text{case (iv)} \end{cases} \tag{7}$$

where

$$\mathbf{S} = \mathbf{O}\cdot\begin{pmatrix} 0 & 0 \\ 0 & 1 \end{pmatrix}\cdot\mathbf{O}^T, \tag{8}$$

reflects the new preferred orientation of cracks in the direction of the most compressive stress and $\mathbf{O}$ is the rotation tensor from the major principal axis of $\mathbf{A}$ to the principal direction of σ associated with σ_1. k_{f} reflects the rate of fracture formation in the sea ice cover and can generally depend on the strain rate as well as on the wind gradient but is here assumed to be a free parameter of the model. In this paper we choose the reference value of $k_{\mathrm{f}} = 10^{-3}\mathrm{s}^{-1}$.

[15] The critical confinement ratio R (where $0 < R < 1$) is also taken as a free parameter of the model. For an homogeneous ice sheet, R is related to the internal friction coefficient, μ_{i}, that appears in Coulomb's phenomenological theory of failure by [*Schulson et al.*, 2006],

$$R = \frac{\left(\mu_i^2 + 1\right)^{1/2} - \mu_i}{\left(\mu_i^2 + 1\right)^{1/2} + \mu_i} \tag{9}$$

and μ_{i} determines the critical Coulombic flaw angle $2\phi = arctan\left(\mu_i^{-1}\right)$, where we have identified the critical angle with the angle ϕ of the diamonds (Figure 1). We identify the parameter k introduced in section 2.1 as the coefficient of friction across a Coulombic fault that is already formed [*Schulson et al.*, 2006], here across the side of the diamond-shaped floes. If we assume that $\mu_{\mathrm{i}} = k$ then the free parameters k, R, and ϕ can be deduced from each other. Some examples of triplets of values are, for increasing values of the angle ϕ, $\{2\varphi = 15°, R = 0.0082\ k = 3.73\}$, $\{30, 0.058, 1.73\}$, $\{60°, 0.36, 0.58\}$ and $\{90°, 1, 0\}$. In reality observations show that the typical angle between intersecting leads in sea ice is around $2\phi = 30° - 40°$ [*Cunningham et al.*, 1994; *Schulson*, 2004].

[16] However, estimates of the internal friction coefficient for sea ice are in contradiction with the Coulomb criterion $2\phi = arctan\left(\mu_i^{-1}\right)$. For example, for $2\phi = 30°$ the theoretical internal friction coefficient is $\mu_i = 1.73$, which contrasts with laboratory estimates of $0.4 < \mu_i < 1$. Reciprocally, a value of $\mu_i = 0.6$ should correspond roughly to a critical angle $2\phi \sim 60°$ and a critical confinement ratio $R \sim 0.3$. It is possible that the lead pairs identified in satellite imagery are not conjugate pairs or that the Coulombic mechanism of failure does not apply. In the winter Arctic, sea ice is anisotropic and contains preexisting frozen leads, that are thinner than the surrounding ice, and can modify the Coulomb theory predictions as described in *Wilchinsky and Feltham* [2011]. Therefore, along with the parameters k_i and k_f, we treat the parameters R, k, and ϕ as independent. The sensitivity of the model to these five parameters is discussed in detail in section 4.

2.3. Ridging, Sliding, and Opening Modes

[17] One of the fundamental challenges in sea ice modeling is to accurately describe the evolution of the ice thickness distribution [*Thorndike et al*., 1975]. During sea ice deformation, ridging, sliding and opening occur simultaneously and their relative contributions depend on the deformation type: for example more sliding occurs in shear than in compression. To resolve the evolution of the ice thickness distribution requires precise knowledge of how much of the deformation is realized through ridging and opening, namely $\alpha_r(\theta)$ and $\alpha_o(\theta)$ [*Thorndike et al*., 1975], and how much goes into sliding $\alpha_s(\theta)$ [*Pritchard*, 1981; *Ukita and Moritz*, 1994]. The angle $\theta = arctan(\dot{\varepsilon}_{II}/\dot{\varepsilon}_I)$ determines the relative amount of shear to divergence and is a function of the ratio of the second and first strain rate invariants (maximum shear rate and divergence, respectively). The ridging mode of deformation was first introduced by *Rothrock* [1975] by relating the rate of doing plastic work by deformation of a unit-thickness sea ice cover to the work done by ridging. This energy balance formulation was then generalized to take into account the contribution to plastic work from sliding [*Ukita and Moritz*, 1994] and from opening [*Wilchinsky et al*., 2006] and reads:

$$\begin{aligned}\sigma_{ij}\dot{\varepsilon}_{ij} &= |\dot{\varepsilon}|(\sigma_I cos\theta + \sigma_{II} sin\theta cos2\gamma) \\ &= |\dot{\varepsilon}|[P_r\alpha_r(\theta) + P_s\alpha_s(\theta) + P_o\alpha_o(\theta)],\end{aligned} \tag{10}$$

where P_r, P_s, and P_o are the ridging, sliding and opening strengths, $\dot{\varepsilon} = \{\dot{\varepsilon}_{ij}\}$ and $\sigma = \{\sigma_{ij}\}$ are the large-scale strain rate and stress tensors, σ_I and σ_{II} are the first and second stress invariants, and γ measures the angle between the major principal axis of the stress with respect to the major principal axis of the strain rate.

[18] To determine the ridging, sliding and opening modes UM considered a simple kinematic model of relative ice floe movement. Here we adopt a different approach and having computed directly the ridging and sliding stress contributions as described section 2.1, we follow *Wilchinsky and Feltham* [2004b] and deduce from equation 10 the ridging and sliding functions,

$$\alpha_r(\theta) = \frac{\sigma_{ij}^r \dot{\varepsilon}_{ij}}{P_r|\dot{\varepsilon}|}, \quad \alpha_s(\theta) = \frac{\sigma_{ij}^s \dot{\varepsilon}_{ij}}{P_s|\dot{\varepsilon}|}. \tag{11}$$

[19] The terms σ_{ij}^r and σ_{ij}^s are the ridging and sliding contribution of the stress tensor defined in equation 3 (the first and second terms on the right hand side, respectively). The opening function is deduced from the kinematic requirement that $\alpha_0(\theta) = cos\theta + \alpha_r(\theta)$.

2.4. Implementation of the New Rheology in CICE

[20] We have incorporated our new model of sea ice rheology into the Los Alamos CICE sea ice model code (version 4.1, freely available online at http://climate.lanl.gov/Models/CICE/), which describes both the thermodynamic and dynamic evolution of the sea ice cover. A description of the Los Alamos CICE sea ice model is contained in the user manual [*Hunke and Lipscomb*, 2008]. As in the original EVP rheology we introduce an artificial elastic response of the strain to a given stress (see section A2) and, by analogy to the EVP rheology, we call our new rheology elastic-plastic-anisotropic (EPA). Elasticity is included not to describe any physical effect, but to make use of an efficient, explicit numerical algorithm used to solve the full sea ice momentum balance and our model should not be confused with models that treat elasticity explicitly [e.g., *Girard et al*., 2011]. The anisotropic stress σ found in section 2.1 is trilinearly interpolated from a previously constructed look-up table for the current values of strain rate and structure tensor (section A1). The look-up table is constructed by computing the stress from equation 2 for discrete values of the largest eigenvalue of the structure tensor, $\frac{1}{2} \le A_1 \le 1$, the angle $0 \le \theta \le 2\pi$ defined in section 2.3, and the angle $-\pi/2 \le y \le \pi/2$ between the major principal axis of the strain rate tensor and the structure tensor. The updated stress, after the elastic relaxation, is then passed to the momentum equation and the sea ice velocities are updated in the usual manner within the subcycling loop of the EVP rheology. The structure tensor evolution equation 5 is solved implicitly at the same frequency, $\delta t_e = 30$ s, as the ice velocities and internal stresses (section A3). Finally, to be coherent with our new rheology we compute the area loss rate due to ridging as $|\dot{\varepsilon}|_r(\theta)$, with $\alpha_r(\theta)$ given by equation 11. Both ridging rate and sea ice strength are computed in the outer loop with a time step $\delta t = 3600$ s.

3. Arctic Basin Scale Simulations

3.1. Reference EVP and EPA Stand-alone Configurations of the Model

[21] The Los Alamos CICE sea ice model (CICE version 4.1) is run in stand-alone mode on a 1° tripolar (129×104) grid that covers the whole Arctic with a horizontal grid resolution of around 40 km. Atmospheric forcing data are taken from the ERA40-based DRAKKAR data set 4 [*Brodeau et al*., 2010]: 6 hourly 10 m winds, 2 m temperatures, and 2 m humidity, daily shortwave and longwave radiation as well as monthly snowfall and precipitation rates. The downward shortwave flux is corrected based on a comparison with Ocean Model Intercomparison Project (OMIP) data [*Röske*, 2006]. Sea surface temperature and salinity are taken from *Ferry et al*. [2011] to initialize the Arctic sea ice state. In addition a mixed layer ocean is applied with climatological prescribed ocean heat flux under the mixed layer from CSSM3 [*Collins et al*., 2006], and the ice-ocean drag is computed from monthly climatological, spatially varying ocean currents of *Ferry et al*. [2011]. Starting with an isotropic homogeneous sea ice with thickness of 2.5 m, a snow depth of 20 cm and

concentration of 100% the model is spun up for 10 years (1980–1989), before producing our analysis simulation for 18 years (1990–2007).

[22] The CICE model with EVP rheology was tuned to match ice concentration data obtained from the Special Sensor Microwave Imager (SSM/I) passive microwave radiometer (Figures 3a, 3b, and 4d). The results were also compared qualitatively with satellite observations of ice thickness (not shown) and ice motion (Figure 8). For the observed ice thickness we used the ERS altimeter-derived data for the months of November to April between 1993 and 2001 below 81.5°N [*Laxon et al*., 2003; *Miller et al*., 2006]. The sea ice drift data were obtained from the Polar Pathfinder Daily 25 km EASE-Grid Sea Ice Motion Vectors data set developed by *Fowler* [2003]. We do not detail here the sensitivity tests that were achieved to obtain the EVP reference run and only give the parameter values used in the reference EVP run. We used the strength parametrization of *Rothrock* [1975] and *Lipscomb et al*. [2007] and fixed the empirical parameter that accounts for frictional energy dissipation to be $C_f = 13$. We fixed the tunable parameter μ_{rdg} that sets the mean ridge height to be $\mu_{rdg} = 4$ m $^{1/2}$ [*Hunke*, 2010]. The parameterization of multiyear ice conductivity, $k_i = 2.03 + 0.13S/T$ (S and T standing for bulk salinity and temperature) was chosen as in *Wettlaufer* [1991]. To calculate the stress between ocean and ice we set the turning angle to zero, used a minimum friction velocity $u^* = 0.0005$ m s $^{-1}$ and an ocean drag coefficient of $c_w = 0.01$. For the rheology we used an elliptical yield curve with a standard value of the squared ratio of the major to minor axes of the elliptical yield curve, $e^2 = 2$. The atmospheric drag as well all remaining parameters of the model were set to the standard values used in the version 4.1 of CICE that was chosen in this work.

[23] In the following section we compare the CICE simulations using the EPA rheology to that obtained using the standard, isotropic EVP rheology. To make the comparison with the EVP run more straightforward, we have normalized the anisotropic stress so that the internal ice stress at pure convergence in the case of isotropically orientated diamonds is equal to the ice stress of the EVP model at pure convergence. Within the EPA rheology it can be shown that the stress at pure convergence in the isotropic case is proportional to $1 + k^2$. Hence to maintain the same stress as in the EVP case we divide the parameter C_f, that sets the ridging strength of the ice, P_r, by $1 + k^2$. In the reference EPA run below (EPA1), where $k = 0.45$, we therefore set $C_f = 10.8$. As will be shown in the following sections the anisotropic simulations at constant compressive stress produce thicker ice on average over the Arctic Basin. To remove the dependence of the other dependent variables on the average thickness in the EPA simulation we produced a second reference run, EPA1*, where $C_f = 21.6$, with an average Arctic Basin scale thickness equal to the thickness in the reference EVP simulation. All other parameters in the reference EPA1 and

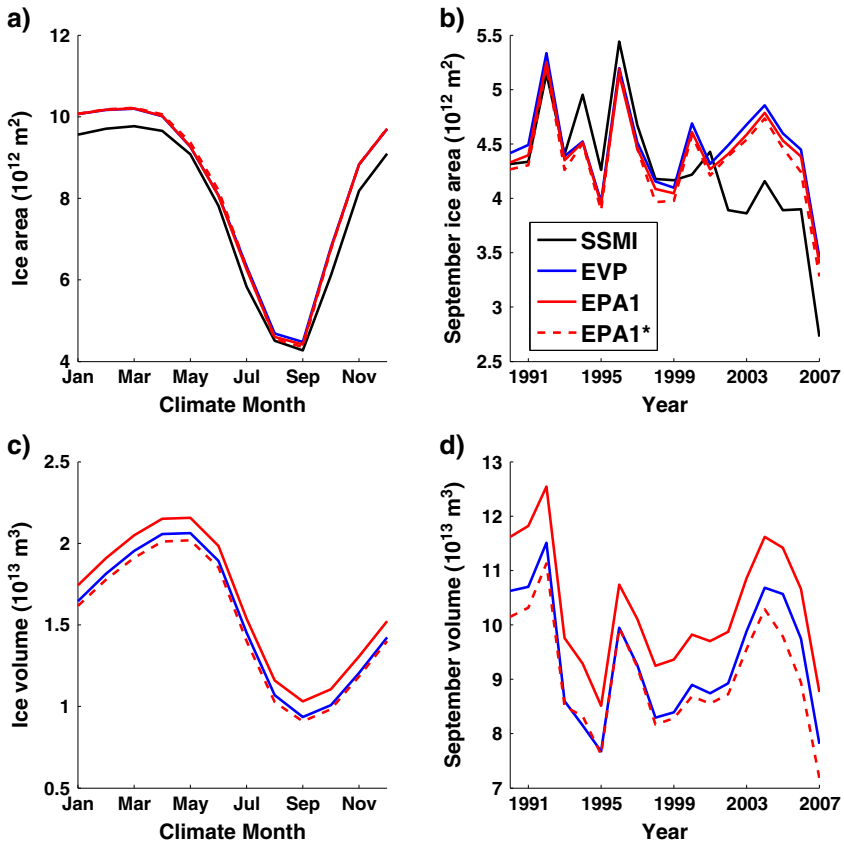

Figure 3. The 1990–2007 mean annual cycles of Arctic (a) ice extent and (c) ice volume. September Arctic (b) ice extent and (d) ice volume. For the ice extent the modeling results of the reference EVP run (blue line) and the reference EPA runs (red line, EPA1, and dotted red line, EPA1*) are compared with passive microwave satellite estimates (SSMI) over the same temporal and spatial windows (black line).

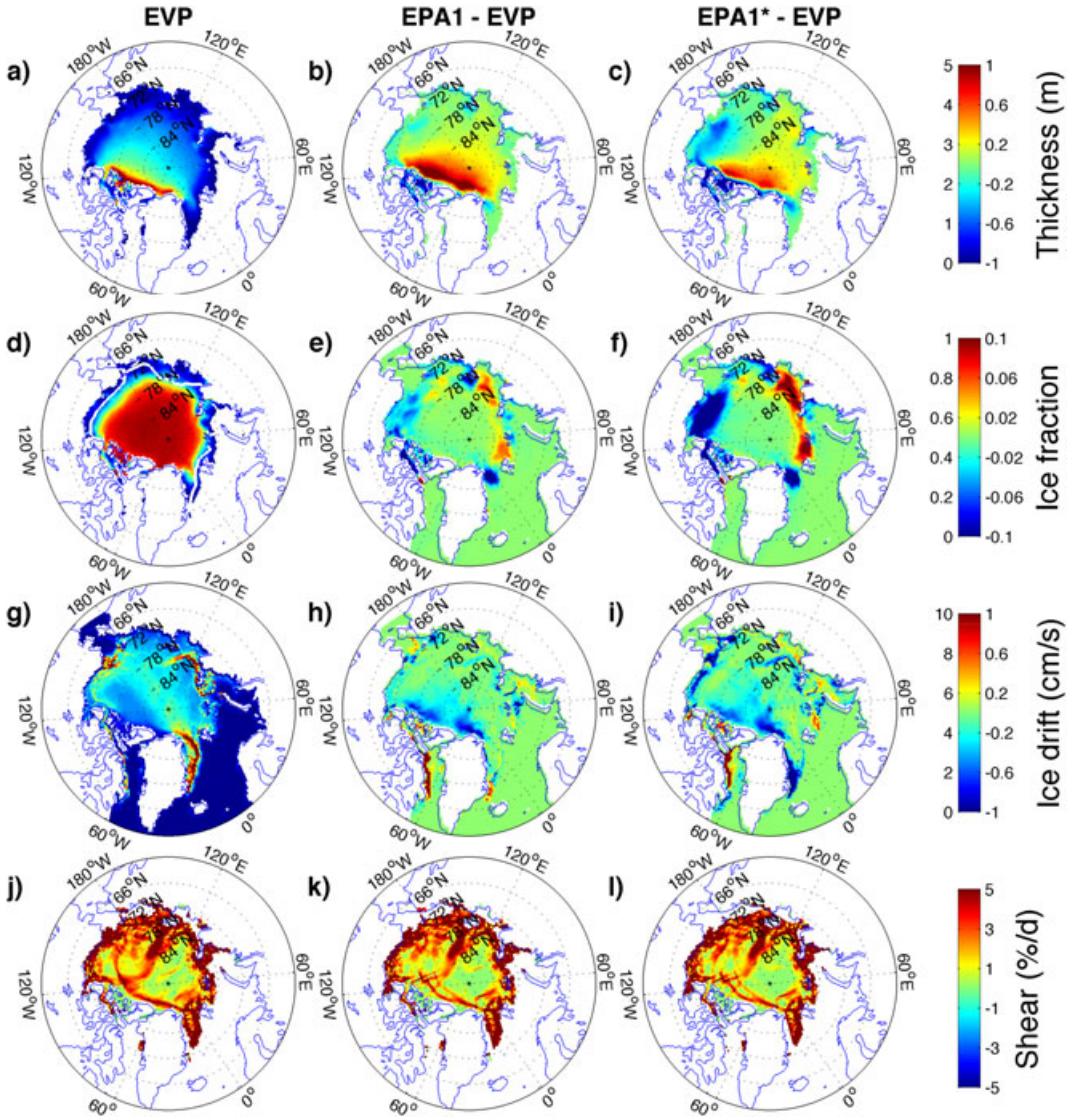

Figure 4. The 1990–2007 climatological September (a) mean ice thickness, (d) mean ice concentration, and (g) mean ice drift for the reference EVP rheology. The white line in Figure 4d shows the September ice extent as measured from passive microwave satellite estimates (SSMI). Same September climatological mean of the difference in (b and c) ice thickness, (e and f) concentration, and (h and i) ice drift between respectively the reference EPA1 and EVP and EPA1* and EVP rheologies. (j–l) Instantaneous shear component of the deformation rate for 1 April 1995. Note the different color scales in all the maps.

EPA1* runs are kept identical to the EVP reference run. In the following sections we first compare the simulation results using the reference EPA and EVP rheologies and then discuss our sensitivity tests with regard to the free parameters of the EPA model, k, k_f, k_i, R and φ, introduced in section 2.

3.2. Influence of Anisotropy on the Sea Ice State and Dynamics

3.2.1. Extent and Area

[24] The climatological seasonal evolution of sea ice extent (Figure 3a) and the evolution of the September ice extent (Figure 3b) over the period 1990 to 2007 show that the EPA rheology introduces only a minor change to the average sea ice extent relative to the EVP run, with the largest deviation being less than 5% in September. Both rheologies reproduce well the observed seasonal average ice extent in the summer season while we attribute a constant overestimation in the winter to erroneous ocean forcing in the Fram Strait. The winter ice extent is determined by oceanic heat flux convergence. If ice is advected into an area with an ocean heat flux of around 200 Wm^{-2} it melts within hours or a few days. In the stand-alone runs, the models do not reproduce the trend of decreasing ice cover in recent years.

[25] The winter ice extent for both EPA and EVP rheologies is mainly constrained in our stand-alone simulation by the strong warm ocean heat fluxes at the Bering and Fram Straits. Therefore only very localized differences in ice concentration can be seen along the ice edge and average to zero when integrated along the ice edge. Looking at characteristic spatial features on the map of Figures 4d–4f, we see that the summer ice extent, on the other hand shows differences with

an increase of ice concentration of up to 10% along the Eastern Arctic ice edge for EPA1 and up to 20% for EPA1*, while the concentrations are reduced again by up to 10% for EPA1 and 20% for EPA1* along most of the Western Arctic ice edge with the ice not penetrating as deeply in the Fram Strait and in the Canadian Archipelago and being particularly depleted in the Beaufort Sea. We see that regions of lower concentration are associated with regions of thinner ice along Alaska, Canada and Greenland while increased concentrations are correlated with increased thickness along the eastern Arctic ice edge. This is visible for both EPA reference runs but is most noticeable for EPA1* on Figures 4c and 4f. We also note that there is no ice concentration difference in the central pack ice signifying that the new ridging and opening rate formulations (see section 2.3) do not modify significantly the concentration of ice (not visible in the maps of Figures 4d–4f, but less than 5%).

3.2.2. Thickness

[26] The climatological data of Figure 3c show that the reference run EPA1 produces on average an additional volume of ice of about $\simeq 2 \cdot 10^{12}$ m ^{3} throughout the year in comparison with the reference EVP run. This corresponds in September to a relative total volume of ice increase of about 20%. The reference run EPA1* was constructed to produce an average thickness over the Arctic Basin similar to the EVP run and as expected the total volume of ice is almost identical. Again, as for the ice extent, the new rheology does not affect the detrended variability of the September total ice volume (Figure 3d). The excess volume of ice in EPA1 is associated with a thicker spatial distribution of ice over a large portion of the Arctic Basin (Figure 4b) with an acute increase of sea ice thickness (up to 2 m) north of the Canadian archipelago and Greenland, while a thinner boundary layer is also visible along the coasts and more drastically in the Canadian archipelago (ice thickness reduced by more than 1 m). While the reference run EPA1* has an average thickness over the entire Arctic Basin that is equal to the average thickness associated with the EVP run, we see in Figure 4c that the spatial distribution of the ice is very different between EPA1* and EVP. In fact EPA1* retains most of the characteristics of EPA1, with thicker ice near the North Pole and thinner ice along the eastern ice edge. These characteristics are in qualitative agreement with ERS satellite and submarine measurements of ice thickness that estimate an overall thicker ice cover (by up to 1 m) with thicker ice near the North Pole and thinner ice in the Beaufort Sea and the Canadian archipelago. Figure 5 shows the average ridging rate over the entire simulation period for the reference EVP run and the differences with the reference EPA runs. While most ridging occurs along the Arctic coast in all simulations, the coastal ridging rate is significantly reduced with the new rheology (particularly with EPA1*). On the other hand the ridging rate north of the Canadian archipelago and near the North Pole is increased by up to 30 cm/year, which corresponds in some areas to a doubling of the ridging rate. The ridging rate is spatially strongly correlated to the total ice thickness in all simulations which highlights the importance of the ridging formulation in the description of the sea ice characteristics.

3.2.3. Anisotropy

[27] Figure 6 illustrates, for two EPA runs with different choices of anisotropy model parameters, how the yield surface depends on the degree of anisotropy of the ice cover. Figures 5a and 5b show, in addition to the standard elliptical yield curve used in the EVP model, cross-sections of the yield surfaces associated with three typical degrees of anisotropy and the flow vectors of angle θ. The theoretical cross sections associated with the isotropic ($A_1 = 0.5$), weakly anisotropic ($A_1 = 0.7$) and strongly anisotropic ($A_1 = 0.9$) cases are represented respectively with the dashed blue, green and red lines. Using the same color scale as for the yield cross-sections we plot snapshot maps of the structure tensor in Figures 6c and 6d. These maps confirm that under realistic forcing the sea ice cover becomes anisotropic over large portions of the Arctic Basin. Most sea ice states realized in the Arctic Basin fall, in the anisotropic cases, on the lower part of the yield cross-section corresponding to orthogonality of the structure and stress tensors, $y = \pi/2$, with $\pi \leq \theta \leq 2\pi$. This means that with the anisotropic rheology the system organizes itself so that the longest axis of the diamond floes lies orthogonal to the most compressive principal stress. By comparing the two runs of Figure 6 we can also see that when the ratio k_f/k_i (the rate of new fracture formation divided by the rate of relaxation to isotropy) is reduced the spread of points becomes larger signifying that the evolution toward orthogonality of stress and structure tensors is restricted, as is expected from equation 5. Note that this is also consistent with equations 7 and 8 that describe the fracturing process of the ice cover leading to alignment of the major principal axes of the structure tensor with the direction of the most compressive stress. In Figures 6e and 6f, the instantaneous orientations over the

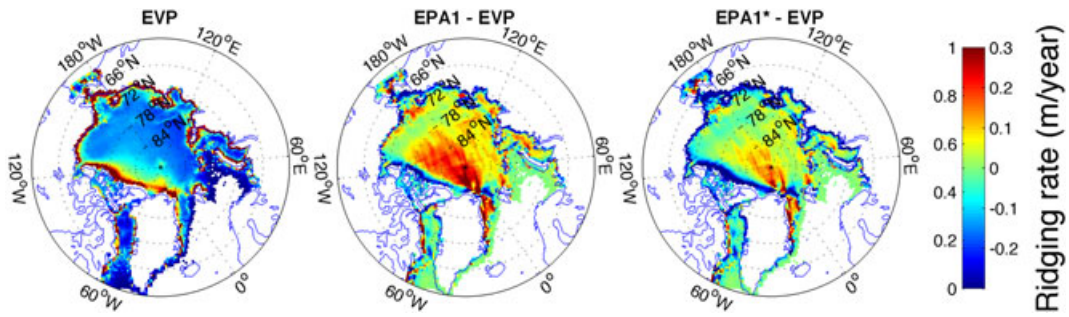

Figure 5. Average ridging rate in m/year for the period January 1990 to December 2007 for the reference EVP run and difference with the reference EPA1 and EPA1* runs. Note the different color scales in all the maps.

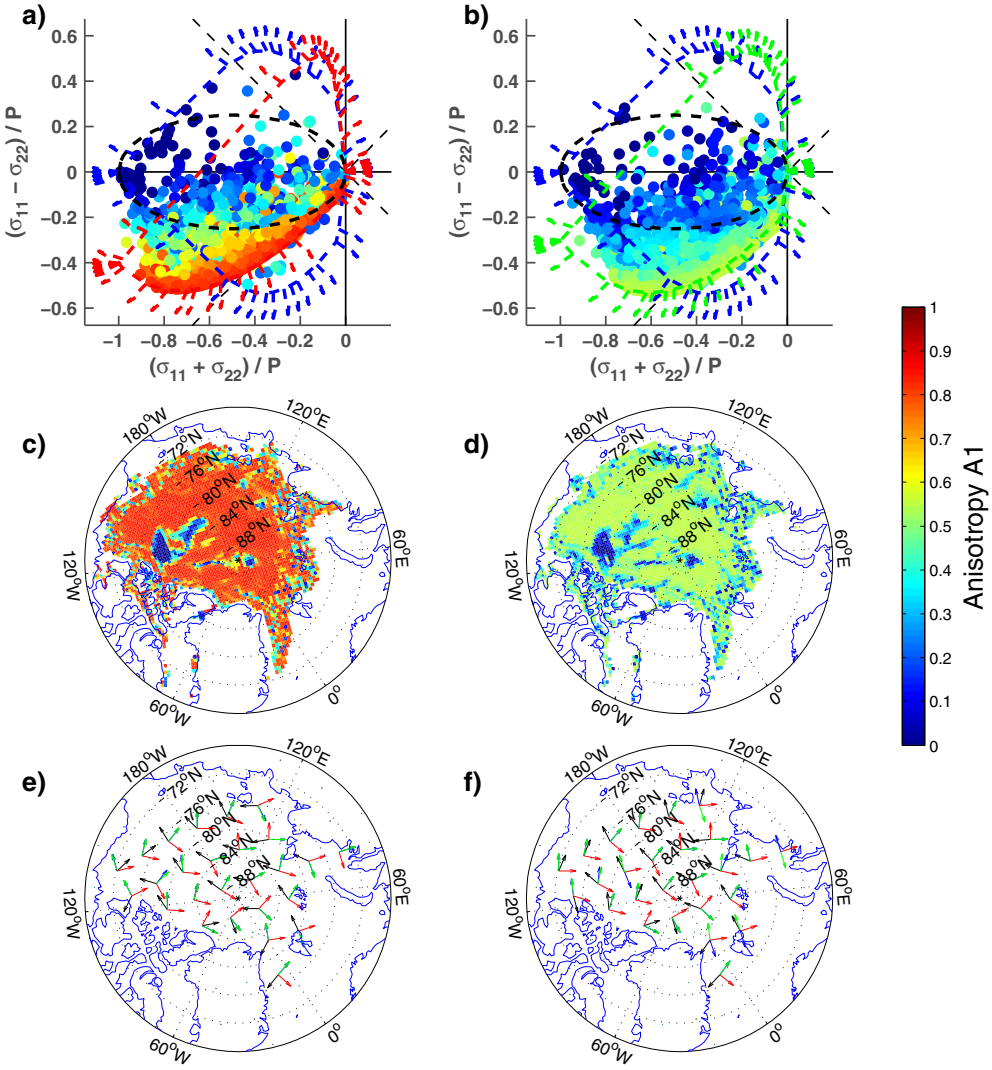

Figure 6. Sea ice stress states over the Arctic Basin for 1 October 1990 for (a) the reference anisotropic EPA1 run (EPA1, $k_f = 1$ and $k_i = 0.2$) and (b) a more isotropic run (EPA2, $k_f = 1$ and $k_i = 1$). The color code is the same for the top four figures and describes the degree of anisotropy of each model grid cell in the Arctic respectively for (c) the reference run and (d) the more isotropic run. In Figures 6a and 6b the black dashed line corresponds to the elliptical EVP yield curve while the blue, green and red dashed lines corresponds to the theoretical cross sections ($y = \pi/2$) of the anisotropic yield surfaces respectively for $A_1 = 0.5$, $A_1 = 0.7$, and $A_1 = 0.9$. The corresponding vectors show the deformation orientation. (e and f) Direction of the major principal axis of the structure tensor (red arrows), strain rate (blue), stress (green), and ice drift (black) for respectively the runs EPA1 and EPA2.

Arctic of the major principal axis of the structure tensor, strain rate tensor and stress tensor along with the ice drift velocity are shown and confirm the overall picture discussed above.

[28] The degree of alignment and the time scale over which sea ice becomes anisotropic are determined respectively by the ratio of k_f/k_i and by the absolute value of these parameters (see also the sensitivity study in section 4). Figure 7a shows three snapshot maps of the instantaneous anisotropy over the Arctic every 12 h over a period of 24 h. The Arctic is predominantly anisotropic but contains quickly evolving regions of isotropic ice. In Figures 7b and 7c we show for a selected grid element of the model the evolution of the structure tensor A_1 and stress ratio σ_1/σ_2 over a period of one week in January 1990. We note that as the ratio σ_1/σ_2 crosses the critical confinement ratio R the structure tensor A_1 relaxes within a few hours to an isotropic state for σ_1/σ_2 R, or to an anisotropic state for $\sigma_1/\sigma_2 < R$. This time scale of a few hours is similar to the time scale of characteristic changes in wind forcing that govern the stress ratio σ_1/σ_2.

3.2.4. Ice Dynamics

[29] In Figures 4g–4i we see that the increase in shear strength associated with the anisotropy of the ice stiffens overall the ice in the basin and reduces the ice drift. This reduction, here shown in September but also seen in spring and early summer, occurs mainly near the coastal regions (Bering Strait, north of Greenland, off the Canadian archipelago, and the Canadian Sea) with a reduction of the ice

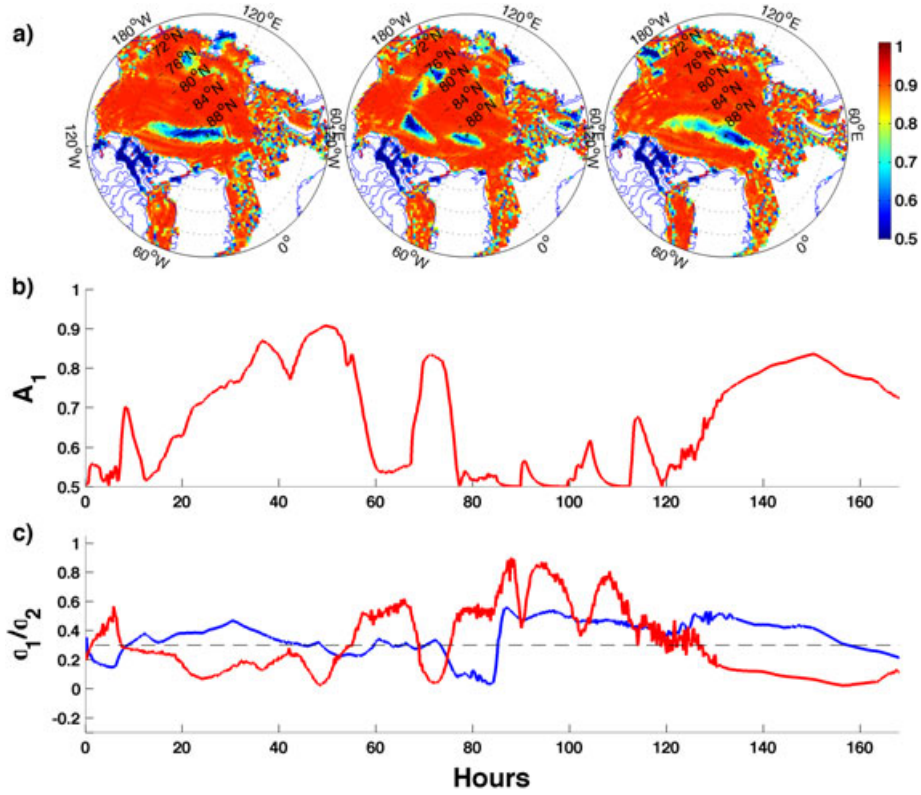

Figure 7. Evolution of the structure and stress tensor: (a) snapshots of the eigenvalue A_1 of the structure tensor. From left to right 48, 60, and 72 h after the initial time of midnight on the 31 of December 1989; (b) Evolution of the eigenvalue A_1 over the first week of 1990; (c) Ratio σ_1/σ_2 of the principal component of the stress tensor for the reference EVP run (blue line) and the reference EPA1 run (red line). The dashed black line indicates the critical confinement ratio $R = 0.3$. The grid cell coordinate analyzed in Figures 7b and 7c is 79°N, 137°W.

drift of up to 2 cm · s $^{-1}$, corresponding to a maximal relative reduction of about 50% north of Greenland where the ice becomes almost immobile during early April. Note that the regions where the ice drift is most reduced correspond to those regions where the ice is thicker on average (Figure 4b). In the reference run EPA1* sea ice drift is reduced further along the east coast of Greenland and off the coast of Alaska.

[30] The time evolution of the average ice drift over the whole Arctic is shown in Figure 8b for the reference EVP and EPA models and compared with the averaged ice drift obtained from the Polar Pathfinder Daily 25 km data set. The Pathfinder data were created by optimally interpolating from Scanning Multichannel Microwave imagery Radiometer, SSM/I, Advanced Very High Resolution Radiometer, and International Arctic Buoy Programme (IABP) data and then averaging to produce a monthly vector field. Here this data set has been regridded onto the model tripolar grid using a Gaussian weighting scheme [*Wilchinsky et al.*, 2006]. Altghough the models were not tuned to fit observed ice velocities, the correlation of speed-time curves, representing the seasonal correlations between the observed and modeled spatially-averaged monthly speed values, appear high (Figure 8b). In accordance with *Wilchinsky et al.*

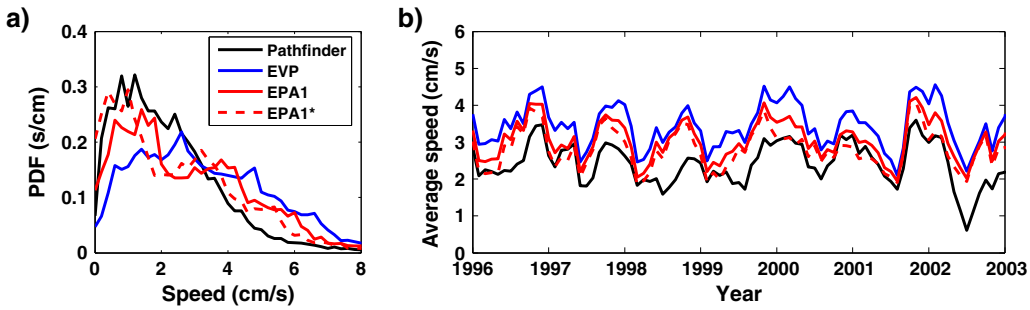

Figure 8. (a) Distribution of ice drift over the Arctic in April for latitudes larger than 78°N, for the Pathfinder data set (black line), the EVP model (blue line), the reference run EPA1 (red line) and the EPA1* run (red dotted line). (b) The time evolution of the average ice speed.

Table 1. Model Parameters Associated With the Different Anisotropic Runs Analyzed in the Paper

Run Index	$k_i \times 10^3$ s^{-1}	$k_f \times 10^3$ s^{-1}	k	R	2ϕ(°)
EPA1	0.2	1	0.45	0.3	30
EPA2	0.8	1	0.45	0.3	30
EPA3	0.05	1	0.45	0.3	30
EPA4	0.2	4	0.45	0.3	30
EPA5	0.2	0.25	0.45	0.3	30
EPA6	0.2	1	0.1	0.3	30
EPA7	0.2	1	1	0.3	30
EPA8	0.2	1	0.45	0.5	30
EPA9	0.2	1	0.45	0.1	30
EPA10	0.2	1	0.45	0.3	90
EPA11	0.2	1	0.45	0.3	15

[2006] we find that generally this correlation between the vector fields is better in the winter months than for the summer months. In addition the new anisotropic rheology reduces the average ice drift and brings it closer to the observed values, with $v_{OBS} = 2.41$ cm·s^{-1}, $v_{EVP} = 3.44$ cm·s^{-1}, $v_{EA1} = 3.05$ cm·s^{-1} and $v_{EA1^*} = 2.81$ cm·s^{-1}, while slightly reducing the correlation, with $R_{OBS/EVP} = 0.86$, $R_{OBS/EA1} = 0.8$ and $R_{OBS/EA1^*} = 0.65$. The improvement with respect to the EVP model is significant in the winter and spring seasons as illustrated from the probability distribution function of the April ice velocities that closely reproduces the observed distribution (Figure 8a), while the improvement is marginal in the Fall and summer seasons (not shown).

4. Sensitivity Study

[31] Having compared the reference EVP and EPA runs, we now discuss how modification of the free parameters of the anisotropic model influence the sea ice behavior. A simple sensitivity study is performed and ten new runs are compared to the reference runs introduced in the previous section. The values allocated to the parameters k_f, k_i, k, R, and ϕ, introduced in section 2 are summarized in Table 1 where one can see that each parameter is allowed to take three distinct values. The simulation results for the various quantities of interest are shown over the Arctic Basin in the Figures 9 to 13. In Table 2 we present, for each

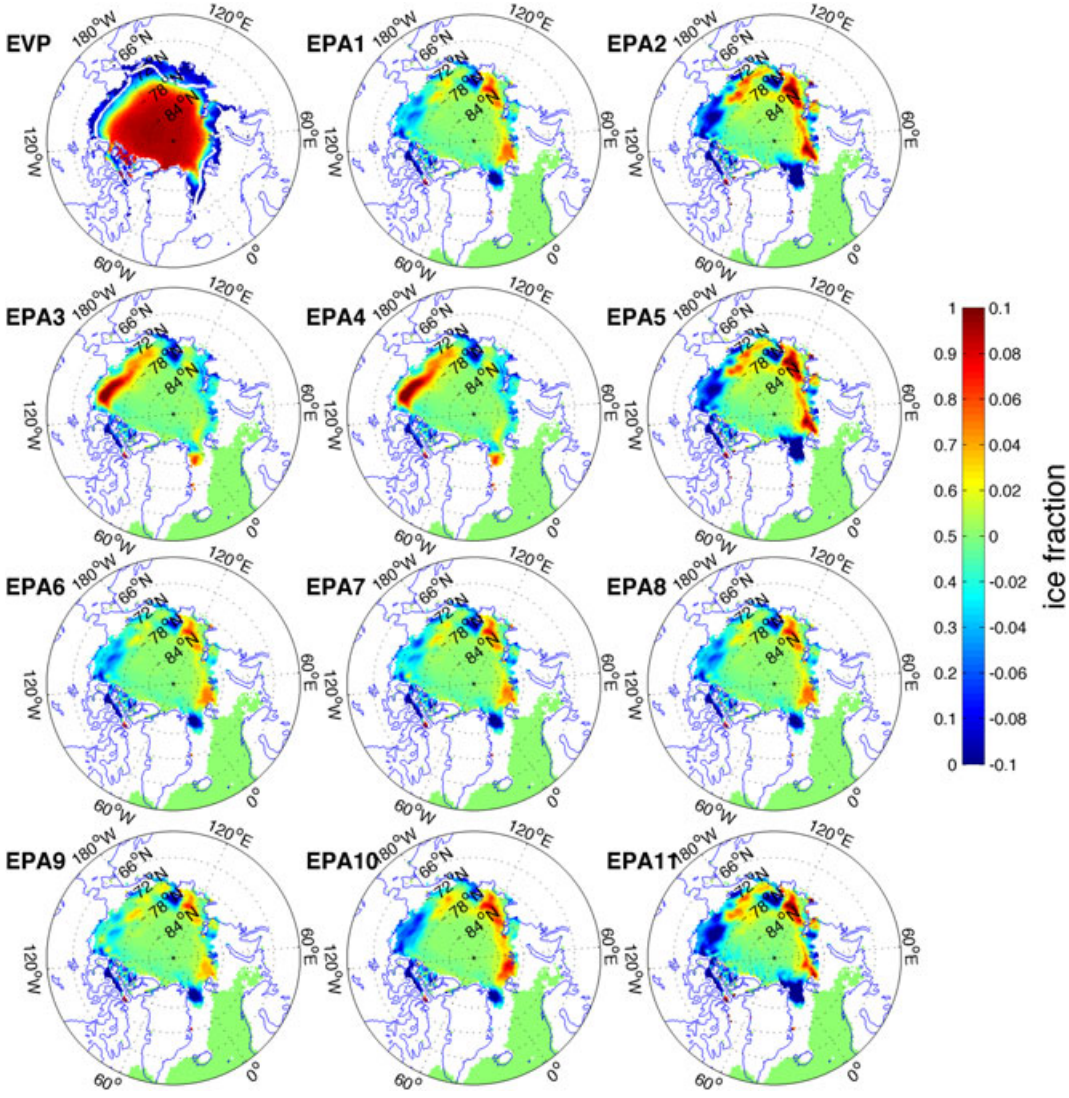

Figure 9. The 1990–2007 climatological September mean ice concentration for the reference EVP rheology and ice concentration difference maps between EPA and EVP for the sensitivity runs EPA1 to EPA11.

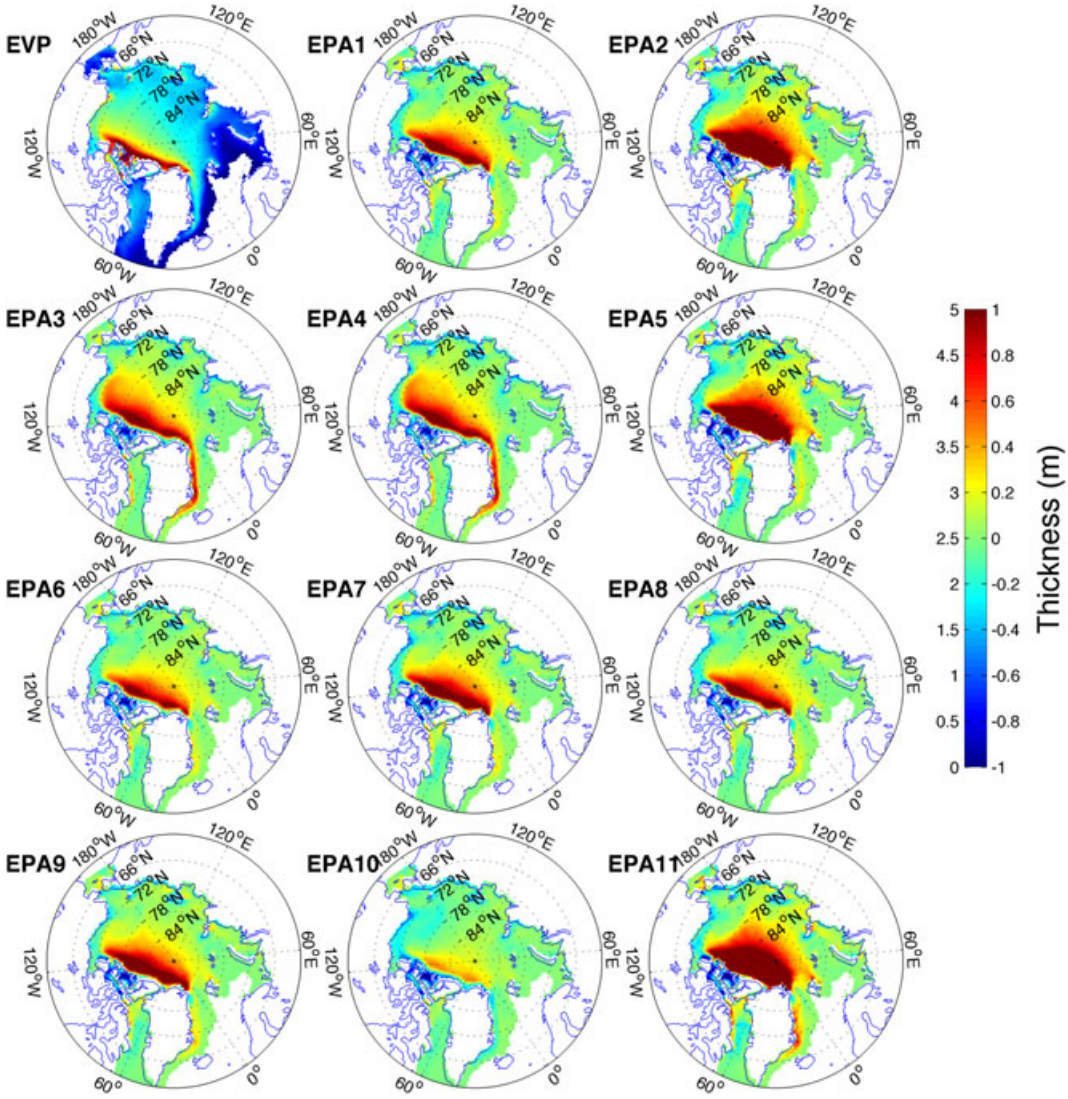

Figure 10. The 1990–2007 climatological March mean ice thickness for the reference EVP rheology and ice thickness difference maps between EPA and EVP for the sensitivity runs EPA1 to EPA11.

sensitivity run, basin-averaged values of thickness, drift speed, structure tensor, stress, and deformation.

4.1. Rate of Fracturing, k_f, Versus Rate of Relaxation to Isotropy, k_i

[32] The values allocated to the parameters k_i and k_f set the relative importance of the two dominant terms, 6 and 7, in the evolution equation of the structure tensor 5 and hence determine the degree of anisotropy of the ice cover. When the ratio k_f/k_i of the rate of new fracture formation over the rate of relaxation to isotropy is reduced from the reference value $k_f/k_i = 5$ (EPA1) to $k_f/k_i = 5/4$ (EPA2 and EPA5), the isotropic contribution to floe reorientation becomes significant and the structure tensor tends to become more isotropic. This appears strikingly on the anisotropy map in Figure 11 where the spatially averaged degree of anisotropy takes the lowest values of the sensitivity study $A_1 = 0.73$ (Table 2). On the other hand when the ratio is increased to $k_f/k_i = 20$ (EPA3 and EPA4), the sea ice cover fractures at a higher rate and becomes highly anisotropic with a maximum averaged anisotropy of $A_1 = 0.89$ (Table 2). In run EPA4 (EPA2) the magnitude of the rates k_i and k_f is multiplied by a factor 4 with respect to the run EPA3 (EPA5) while the ratio $k_f/k = 20$ ($k_f/k_i = 5/4$) is kept the same. The simulations that have the same ratio are almost identical (compare EPA2 with EPA5 and EPA3 with EPA4) and only differ by the time scale over which ice floes reorientate to adjust to the changing external forcing conditions. For the rate parameters chosen here this happens in both cases within less than an hour, which in comparison with the several hour time scale associated with the wind forcing, is negligible. It is also noteworthy that the highly anisotropic runs EPA3 and EPA4 display a markedly different spatial organization of the ice concentration (Figure 9) and thickness (Figure 10), with thicker ice extending in spring further along the Greenland and Alaska coasts. We attribute this effect to the fact that in strongly anisotropic runs the model produces thicker ice than in the reference EVP run without reducing the drift of the ice (Figure 12), resulting in a strong advection of ice associated with the transpolar drift and Beaufort Gyre.

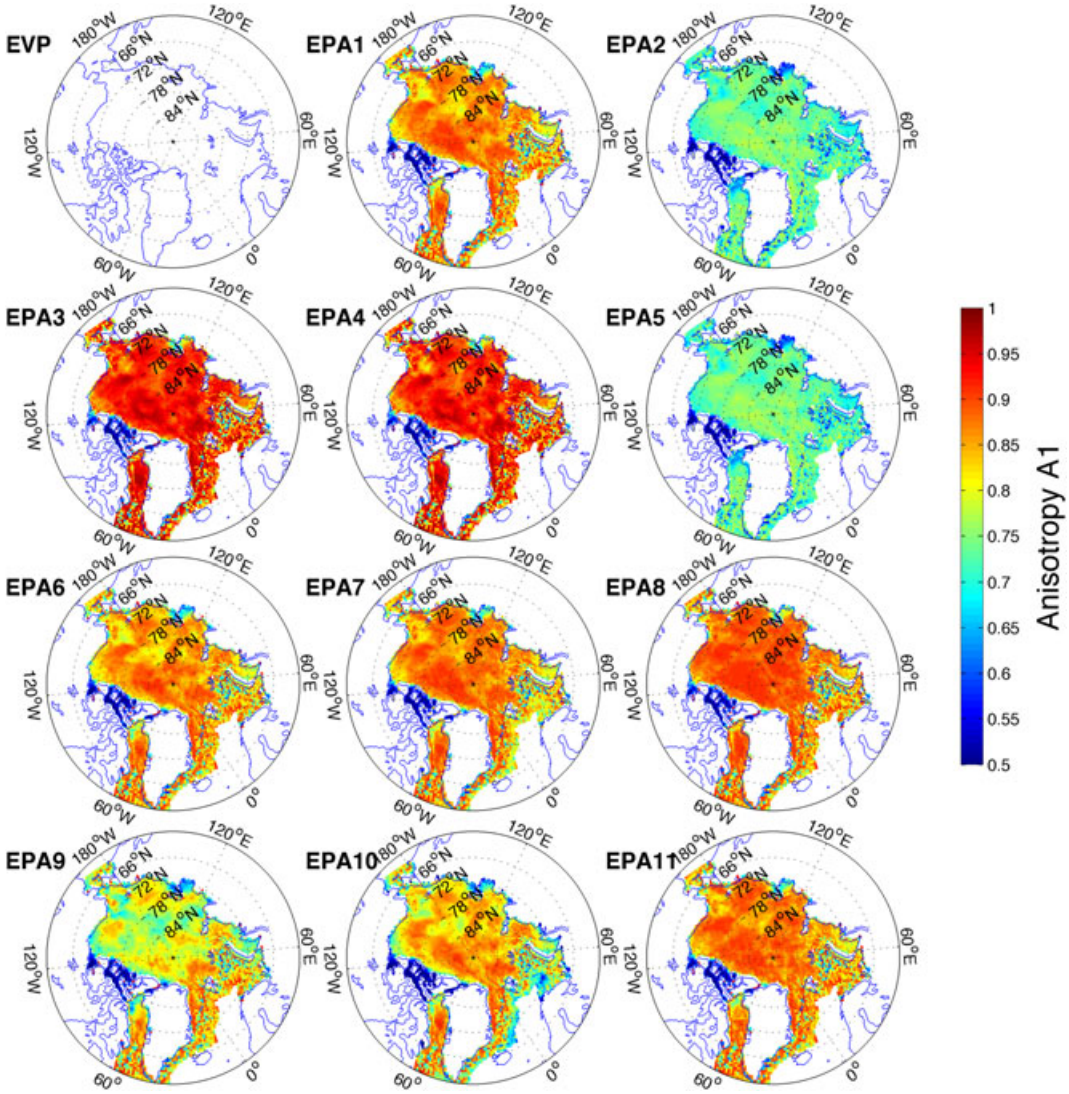

Figure 11. The 1990–2007 climatological March ice anisotropy maps for the sensitivity runs EPA1 to EPA11. Note that the EVP run has no anisotropy associated.

4.2. Contribution to Sea Ice Stress From Sliding Versus Ridging, k

[33] As discussed in section 2.1 the friction parameter k sets the relative magnitude of the sliding and ridging forces at the contact between ice floes. By modifying the friction parameter k, the shape of the yield surface changes along with the partition of the energy dissipated in ridge building and frictional sliding. For low values of k the yield stress will be dominated by the ridging contribution while as k is increased the sliding contribution becomes increasingly significant, see equation 3. For a small friction parameter ($k = 0.1$), Figure 13 EPA6 shows that the yield curve is restricted to stresses with $\sigma_I < 0$ and has a reduced magnitude of the maximum shear stress σ_{II} for the anisotropic cases. Figure 13 EPA7 shows that for a larger friction coefficient ($k = 1$) the yield curve for the isotropic cases is largely unaffected but in the anisotropic cases there is a decrease of the normal stress (σ_2) across the direction of floe alignment and a near alignment with the σ_1 axis. This is an expected behavior, as the sliding stress is directed along the floe edges, and, as the degree of alignment grows, the floe edges tend to lie closer to the alignment direction than across it. It is interesting to note that modifying k does not have the same influence on the sea ice as reducing the ratio k_f/k_i, and, as summarized in table 2 and Figures 9 to 13, leaves most significant fields such as ice thickness, drift, shear stress and anisotropy roughly unchanged with respect to the reference EPA1 run.

4.3. Critical Confinement ratio, R, and Tiling Geometry, ϕ

[34] We modify the parameter R from its reference value $R = 0.3$ to the values $R = 0.5$ and $R = 0.1$, respectively, in EPA8 and EPA9 in Figures 9 to 13. As R is reduced it becomes progressively harder for the ice stress principal components to satisfy the condition $\sigma_1/\sigma_2 < R$ (equation 8) so less Coulombic fracturing occurs and the ice becomes more isotropic. This reduction of the anisotropy over the Arctic as R is reduced is visible in Figure 11, EPA9. As expected from the shape of the yield curves (Figure 13) reducing R is also accompanied by a decrease of the absolute

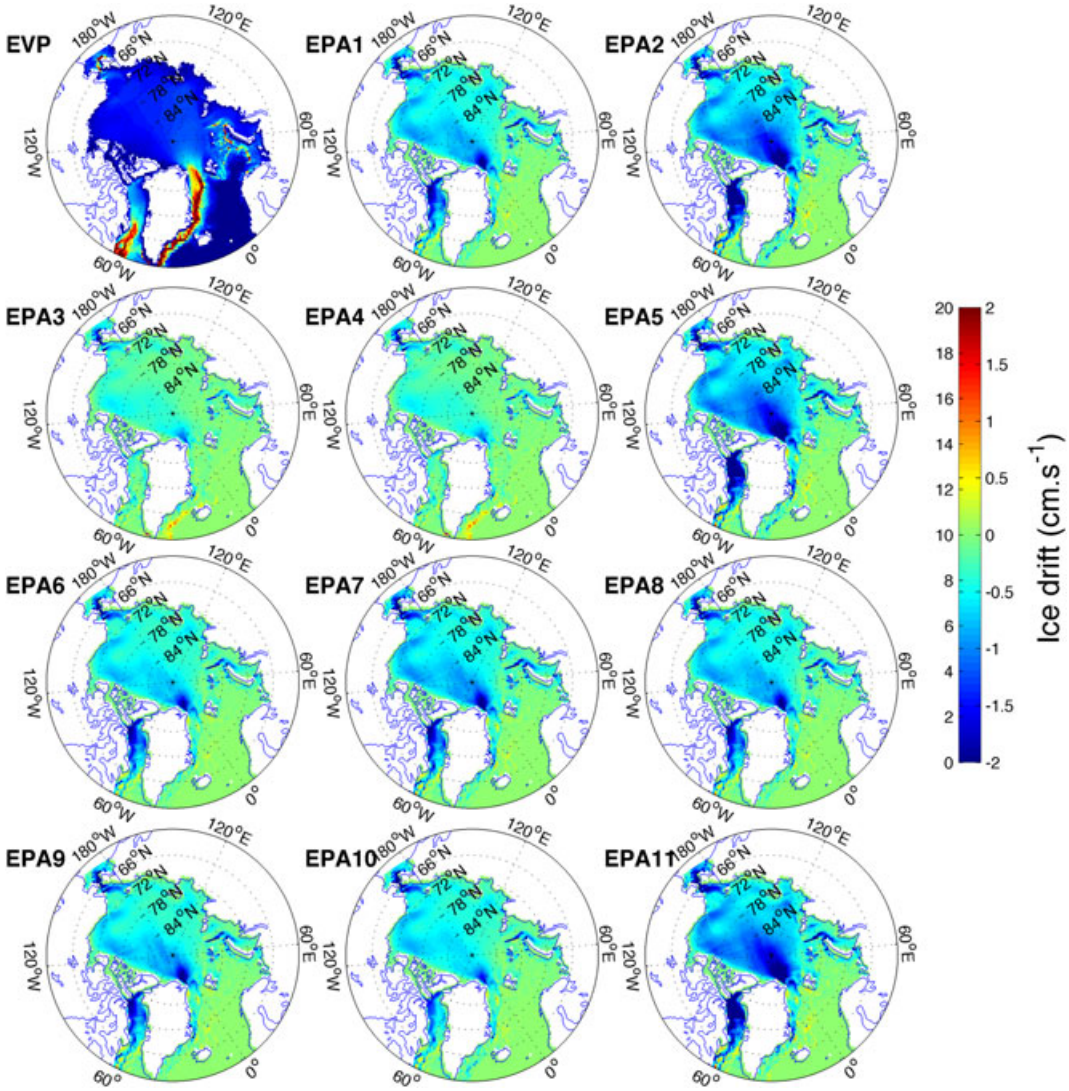

Figure 12. The 1990–2007 climatological March mean ice drift for the reference EVP rheology and ice drift difference maps between EPA and EVP for the sensitivity runs EPA1 to EPA11.

value of the average shear stress and pressure together with a slight increase of the average ice thickness and drift (Table 2).

[35] Turning now to the parameter ϕ we see that changing the acute angle of the diamond shaped floes has an even more dramatic impact on the yield curve shape. For square shaped floes, $2\phi = 90°$, (Figure 13, EPA10) for both isotropic and anisotropic cases the yield curve is confined to $\sigma_1 < 0$ with a sea ice cover that cannot sustain tensile stresses. On the other hand for more acute angles, $2\phi = 15°$, Figure 13 EPA11 shows that the yield curves become wider with a large shear strength and almost a quarter of sea ice stresses in the tensile portion, $\sigma_1 > 0$. The impact of this on both thickness and sea ice drift is dramatic (Figures 10 and 12) and highlights the pattern already seen above that yield curves with large tensile component ($\sigma_1 > 0$) generate thicker and stiffer ice.

5. Summary and Concluding Remarks

[36] We have implemented a new anisotropic rheology of the sea ice cover into the sea ice component of a global circulation model. The implementation process is straightforward, with the new anisotropy model taking the form of a module that can be switched on or off, and, although not yet optimized for large-scale computation, the anisotropy model is computationally efficient. While the model of anisotropy is phenomenological, it is supported by existing theory. In addition to providing a subcontinuum rationale for the continuum scale stresses, the anisotropic rheology evolves to produce a range of stress states, encompassing rheological choices previously introduced as fixed for the entire pack and independent of time, for example yield curves with large shear to compression ratio or with a biaxial tensile stress component. The results of modeling the sea ice cover over a large region of the Arctic Ocean with a standalone simulation showed that under realistic forcing the sea ice reaches a predominantly anisotropic state, as confirmed from remote sensing observations. Although the aim of this paper was not to calibrate the anisotropic rheology to fit observations, it appears that the proposed model also performs well in reproducing the observed ice concentration, ice thickness and ice drift

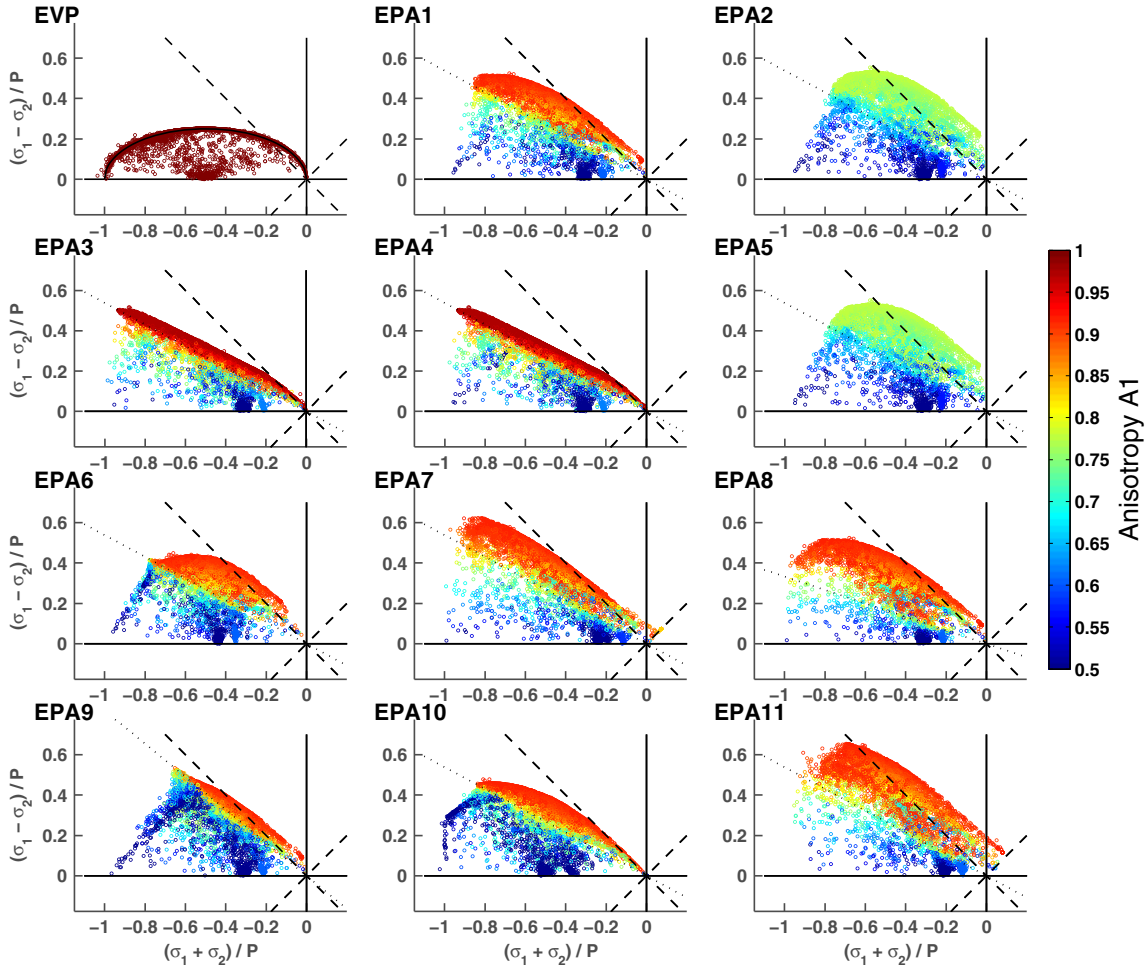

Figure 13. Sea ice stress states over the Arctic Basin for 1 April 1995 for the reference EVP run and the sensitivity runs EPA1 to EPA11. The color code represents for each grid point the associated degree of anisotropy.

Table 2. Characteristics of 18 year Sensitivity Experiments Averaged Over Entire Year. The Average Values of Each Field is Computed Over the Entire Arctic Basin Where the Ice Thickness is Larger Than 10 cm. In Parenthesis is Computed the Variance of Each Quantity

Run Index	Thickness (m)	Ice drift (cm · s $^{-1}$)	Structure Tensor A_1	Pressure/Shear Stress (kN · m $^{-2}$)	Divergence/Shear (10 $^{-7}$ s $^{-1}$)
EVP	1.72 (0.78)	3.73 (4.37)	-	–9.8 (12.7) / 3.7 (4.2)	0 (1.8) / 2.4 (3.7)
EPA1	1.83 (1.22)	3.39 (4.28)	0.84 (0.12)	–9.7 (11.7) / 6.5 (8.0)	0 (1.8) / 2.1 (3.6)
EPA2	1.99 (1.42)	3.22 (4.25)	0.73 (0.08)	–9.6 (12.7) / 8.0 (10.5)	0 (1.8) / 2.1 (3.6)
EPA3	1.85 (1.22)	3.61 (4.36)	0.89 (0.13)	–8.9 (11.3) / 4.9 (6.1)	0 (1.8) / 2.3 (3.7)
EPA4	1.85 (1.22)	3.61 (4.36)	0.89 (0.14)	–8.9 (11.2) / 4.8 (6.1)	0 (1.8) / 2.3 (3.7)
EPA5	1.99 (1.42)	3.22 (4.25)	0.73 (0.08)	–9.6 (12.7) / 8.0 (10.5)	0 (1.8) / 2.0 (3.7)
EPA6	1.81 (1.20)	3.44 (4.29)	0.83 (0.12)	–10.2 (12.3) / 6.3 (7.5)	0 (1.8) / 2.1 (3.6)
EPA7	1.86 (1.26)	3.37 (4.27)	0.84 (0.11)	–9.2 (11.6) / 6.7 (8.5)	0 (1.8) / 2.1 (3.6)
EPA8	1.82 (1.22)	3.39 (4.28)	0.85 (0.11)	–9.8 (11.8) / 6.6 (8.0)	0 (1.8) / 2.1 (3.6)
EPA9	1.88 (1.29)	3.42 (4.29)	0.79 (0.14)	–9.1 (11.1) / 6.4 (7.9)	0 (1.8) / 2.1 (3.7)
EPA10	1.70 (1.08)	3.45 (4.27)	0.81 (0.14)	–11.1 (13.6) / 6.0 (7.2)	0 (1.7) / 2.1 (3.6)
EPA11	2.06 (1.51)	3.20 (4.27)	0.84 (0.11)	–9.0 (12.7) / 8.0 (11.2)	0 (1.8) / 2.0 (3.7)

spatial patterns over the Arctic. We find that, all other things being equal, introducing the anisotropic rheology produces a thicker yield curve with an overall ice thickness increase and ice drift reduction over the Arctic Basin. If we normalize the anisotropic yield curve to produce an average ice thickness over the Arctic Basin comparable to that calculated with the reference EVP model we find that significant spatial differences remain in the distribution of the ice thickness and ice drift over the Arctic Ocean. The anisotropic ice drift is reduced on average, particularly along the western coast of the Arctic Ocean, and the ice thickness is increased near the North Pole and reduced in the Beaufort Sea. These results constitute an improved representation of the observed sea ice state and dynamics over

the period of study. We have presented a sensitivity study indicating how the free parameters of the anisotropic model influence the sea ice behavior. To keep the model as simple as possible, we considered these parameters to be constant in space and time. Various refinements to this approach are possible and could be implemented straightforwardly. In the sensitivity study we showed that modifying the ratio of the rate of fracturing to the rate of relaxation to isotropy, k_f/k_i, the critical confinement ratio, R, the tiling geometry, ϕ, and to a lesser degree the relative contribution to sea ice stress from sliding versus ridging, k, results in a change in the shape of the anisotropic yield curve that can explain the modified sea ice characteristics. Calibration of the model against forthcoming ice thickness map measurements extending to high latitudes over the polar regions from Cryosat2 is an exciting extension of this work. Another important extension of this work will consist in testing the model in coupled sea-ice ocean simulations at higher resolutions. We believe that this new rheology can shed new light on the feedback mechanism that takes place between the Arctic sea ice thickness and the ice drift, through a better understanding of its mechanical properties.

Appendix A
Model Implementation

A.1. Look-up Tables

[37] Here we describe how the look-up table associated to the anisotropic stress is calculated for discrete values of the largest eigenvalue of the structure tensor, $\frac{1}{2} \leq A_1 \leq 1$, the angle $0 \leq \theta \leq 2\pi$ defined in section 2.3, and the angle $-\pi/2 \leq y \leq \pi/2$ between the major principal axis of the strain rate tensor and the structure tensor. The unit vectors are expressed as:

$$\mathbf{n}_1(z,\theta) = (cos(z+\pi/2-\varphi), sin(z+\pi/2-\phi)), \tag{A.1}$$

$$\mathbf{n}_2(z,\theta) = (cos(z-\pi/2+\phi), sin(z-\pi/2+\phi)), \tag{A2}$$

$$\tau_1(z,\theta) = (cos(z-\phi), sin(z-\phi)), \tag{A3}$$

$$\tau_2(z,\theta) = (cos(z+\phi), sin(z+\phi)), \tag{A4}$$

where the unit vectors and the angles are defined in Figure 2.

[38] Now, with the strain rate principal components defined as $\dot{\varepsilon}_1(\theta) = |\dot{\varepsilon}| cos(\theta)$ and $\dot{\varepsilon}_2(\theta) = |\dot{\varepsilon}| sin(\theta)$, the strain-rate components in the coordinate system associated to the major principal axis of the structure tensor are00

$$\dot{\varepsilon}_{11}(\theta,y) = cos^2 y\left(\dot{\varepsilon}_1(\theta) + \dot{\varepsilon}_2(\theta) tan^2 y\right), \tag{A5}$$

$$\dot{\varepsilon}_{12}(\theta,y) = cos^2 y tany(-\dot{\varepsilon}_1(\theta) + \dot{\varepsilon}_2(\theta)), \tag{A6}$$

$$\dot{\varepsilon}_{22}(\theta,y) = cos^2 y\left(\dot{\varepsilon}_2(\theta) + \dot{\varepsilon}_1(\theta) tan^2 y\right). \tag{A.7}$$

[39] Replacing equations A.1 to A.7 in equation 2 one obtains the ridging, $\sigma_r^b(\theta,y,z)$, and sliding, $\sigma_s^b(\theta,y,z)$, functions. These are then multiplied by $\psi(A_1,z)$ and integrated over z to produce the look-up tables $\sigma_r(A_1,\theta,y)$ and $\sigma_s(A_1,\theta,y)$. These look-up table values are then trilinearly extrapolated in CICE and multiplied as in equation 3 by the ridging and sliding strength to produce the anisotropic stress σ.

A.2. Stress Tensor Evolution Equation

[40] Here we follow [*Hunke and Lipscomb*, 2008] and formulate the stress tensor σ in terms of $\sigma_1 = \sigma_{11} + \sigma_{22}$, $\sigma_2 = \sigma_{11} - \sigma_{22}$. We replace the stress equations of the latest version of the EVP dynamics,

$$\frac{\partial \sigma_1^{\mathrm{EVP}}}{\partial t} + \frac{\sigma_1^{\mathrm{EVP}}}{2T} + \frac{P}{2T} = \frac{P}{2T\Delta} D_D, \tag{A8}$$

$$\frac{\partial \sigma_2^{\mathrm{EVP}}}{\partial t} + \frac{e^2 \sigma_2^{\mathrm{EVP}}}{2T} + \frac{P}{2T} = \frac{P}{2T\Delta} D_T, \tag{A9}$$

$$\frac{\partial \sigma_{12}^{\mathrm{EVP}}}{\partial t} + \frac{e^2 \sigma_{12}^{\mathrm{EVP}}}{2T} + \frac{P}{2T} = \frac{P}{4T\Delta} D_S, \tag{A10}$$

where we use the divergence $D_D = \dot{\varepsilon}_{11} + \dot{\varepsilon}_{22}$, the tension $D_T = \dot{\varepsilon}_{11} - \dot{\varepsilon}_{22}$ and shearing strain rate $D_S = 2\dot{\varepsilon}_{12}$ with the analogous EPA stress equations,

$$\frac{\partial \sigma_1^{\mathrm{EPA}}}{\partial t} + \frac{\sigma_1^{\mathrm{EPA}}}{2T} = \frac{\sigma_1}{2T}, \tag{A12}$$

$$\frac{\partial \sigma_2^{\mathrm{EPA}}}{\partial t} + \frac{\sigma_2^{\mathrm{EPA}}}{2T} = \frac{\sigma_2}{2T}, \tag{A13}$$

$$\frac{\partial \sigma_{12}^{\mathrm{EPA}}}{\partial t} + \frac{\sigma_{12}^{\mathrm{EPA}}}{2T} = \frac{\sigma_{12}}{2T}. \tag{A14}$$

σ is the anisotropic stress tensor deduced from the look-up table described in the previous section and T is the same damping timescale that is introduced in CICE.

A.3. Structure Tensor Evolution Equation

[41] The new anisotropic rheology requires to solve, in addition to the momentum and stress equations, the evolution equation 8 for the structure tensor. As stated in section 2.3, equation 8 is solved within the subcycling loop of the EVP rheology and, consistently with the momentum and stress evolution equations, we neglect the advection term for the structure tensor. Neglecting also the mechanical contribution F_{mech}, equation 8 consists of the simplified system of two equations:

$$\frac{\partial A_{11}}{\partial t} = -k_t\left(A_{11} - \frac{1}{2}\right) + M_{11}, \tag{A16}$$

$$\frac{\partial A_{12}}{\partial t} = -k_t A_{12} + M_{12}, \tag{A16}$$

where M_{11} and M_{12} are the components of the term F_{frac} in equation 10. These equations are discretized in time semi-implicitly as

$$\frac{1}{\Delta t}\left(A_{11}^{k+1} - A_{11}^{k}\right) = -k_t\left(A_{11}^{k+1} - \frac{1}{2}\right) + M_{11}^{k}, \tag{A17}$$

$$\frac{1}{\Delta t}\left(A_{12}^{k+1} - A_{12}^{k}\right) = -k_t A_{12}^{k+1} + M_{12}^{k}, \tag{A18}$$

where k denotes the subcycling time step and the fracture terms are computed at the previous step.

[42] **Acknowledgments.** We are grateful to R. Pritchard and J. Hutchings as well as to one anonymous reviewer for helpful comments on an earlier version of our paper. We deeply thank D. Schröder for producing the reference EVP run used in the paper.

References

Brodeau, L., B. Barnier, A.-M. Treguier, T. Penduff, and S. Gulev (2010), An era40-based atmospheric forcing for global ocean circulation models, *Ocean Modelling*, *31*(3-4), 88–104.

Collins, W., *et al*. (2006), The community climate system model version 3 (ccsm3), *Journal of Climate*, *19*(11), 2122–2143.

Coon, M., G. Maykut, and R. Pritchard (1974), Modeling the pack ice as an elastic-plastic material, *AIDJEX Bull*.

Coon, M., G. Knoke, D. Echert, and R. Pritchard (1998), The architecture of an anisotropic elastic-plastic sea ice mechanics constitutive law, *Journal of Geophysical Research-Oceans*, *103*(C10), 21915–21925.

Coon, M., R. Kwok, G. Levy, M. Pruis, H. Schreyer, and D. Sulsky (2007), Arctic ice dynamics joint experiment (aidjex) assumptions revisited and found inadequate, *Journal of Geophysical Research-Oceans*, *112*(C11), C11S90, doi:10.1029/2005JC003393.

Cunningham, G., R. Kwok, and J. Banfield (1994), Ice lead orientation characteristics in the winter beaufort sea, in *Geoscience and Remote Sensing Symposium*, *1994. IGARSS '94. Surface and Atmospheric Remote Sensing*: *Technologies*, *Data Analysis and Interpretation*., *International*, vol. 3, pp. 1747–1749 vol.3.

Feltham, D. (2008), Sea ice rheology, doi:10.1146/annurev.fluid.40.111406.102151.

Ferry, N., S. Masina, A. Storto, K. Haines, M. Valdivieso, B. Barnier, and J.-M. Molines (2011), Product user manual global-reanalysis-phys-001-004-a and b, myocean., *Tech. rep*.

Fowler, C. (2003), Polar pathfinder daily 25 km ease-grid sea ice motion vectors, http://nsidc.org/data/nsidc-0116.html, natl. snow and ice data cent., boulder, colo.

Girard, L., S. Bouillon, J. Weiss, D. Amitrano, T. Fichefet, and V. Legat (2011), A new modeling framework for sea-ice mechanics based on elasto-brittle rheology, *Annals of Glaciology*, *52*(57), 123.

Hibler III, W. (1979), A dynamic thermodynamic sea ice model, *Journal of Physical Oceanography*, *9*(4), 815–846, doi:10.1175/1520-0485.

Hibler III, W. (2001), Sea ice fracturing on the large scale, *Engineering Fracture Mechanics*, *68*(17-18), 2013 – 2043, doi:10.1016/S0013-7944(01)00035-2.

Hibler III, W., and E. Schulson (2000), On modeling the anisotropic failure and flow of flawed sea ice, *Journal of Geophysical Research-Oceans*, *105*(C7).

Hopkins, M., S. Frankenstein, and A. Thorndike (2004), Formation of an aggregate scale in arctic sea ice, *Journal of Geophysical Research*, *109*(C1), C01,032, doi:10.1029/2003JC001855.

Hunke, E., and W. Lipscomb (2008), Cice: The los alamos sea ice model, documentation and software user's manual, version 4.0., *Los Alamos National Laboratory Tech. Rep. LA-CC-06-012*.

Hunke, E. C. (2010), Thickness sensitivities in the cice sea ice model, *Ocean Modelling*, *34*(3-4), 137–149.

Kreyscher, M., M. Harder, P. Lemke, and G. Flato (2000), Results of the sea ice model intercomparison project: Evaluation of sea ice rheology schemes for use in climate simulations, *Journal of Geophysical Research-Oceans*, *105*(C5).

Kwok, R., E. C. Hunke, W. Maslowski, D. Menemenlis, and J. Zhang (2008), Variability of sea ice simulations assessed with rgps kinematics, *Journal of Geophysical Research-Oceans*, *113*, C11,012, doi:10.1029/2008JC004783.

Laxon, S., N. Peacock, and D. Smith (2003), High interannual variability of sea ice thickness in the arctic region, *Nature*, *425*(6961), 947–950.

Lipscomb, W., E. Hunke, W. Maslowski, and J. Jakacki (2007), Ridging, strength, and stability in high-resolution sea ice models, *J. Geophys. Res*, *112*, doi:10.1029/2005JC003355.

Marsan, D., H. Stern, R. Lindsay, and J. Weiss (2004), Scale dependence and localization of the deformation of arctic sea ice, *Physical review letters*, *93*(17), 178,501.

Miller, P., S. Laxon, and D. Feltham (2005), Improving the spatial distribution of modeled arctic sea ice thickness, *Geophys. Res. Lett*, *32*, 18.

Miller, P., S. Laxon, D. Feltham, and D. Cresswell (2006), Optimization of a sea ice model using basinwide observations of arctic sea ice thickness, extent, and velocity, *Journal of Climate*, *19*(7), 1089–1108, doi:10.1175/JCLI3648.1.

Moritz, R., and J. Ukita (2000), Geometry and the deformation of pack ice: I. a simple kinematic model, *Annals of Glaciology*, *31*(1), 313–322.

Pritchard, R. (1981), Mechanical behavior of pack ice, *Mechanics of structured media. Pt A./Ed. APS Selvadurai*. Amsterdam: Elsevier, pp. 371–05.

Pritchard, R. (1998), Ice conditions in an anisotropic sea ice dynamics models, *International Journal of Offshore and Polar Engineering*, *8*(1), 9–15.

Pritchard, R. S. (2001), Long-term sea ice dynamics simulations using an elastic-plastic constitutive law, *J. Geophys. Res.*, *106*(C12), 31,333–31,343.

Rampal, P., J. Weiss, C. Dubois, and J.-M. Campin (2011), Ipcc climate models do not capture arctic sea ice drift acceleration: Consequences in terms of projected sea ice thinning and decline, *J. Geophys. Res.*, *116*, C00D07–.

Röske, F. (2006), A global heat and freshwater forcing dataset for ocean models, *Ocean Modelling*, *11*(3-4), 235–297.

Rothrock, D. (1975), The energetics of the plastic deformation of pack ice by ridging, *Journal of Geophysical Research-Oceans*, *80*(33).

Schreyer, H. L., D. L. Sulsky, L. B. Munday, M. D. Coon, and R. Kwok (2006), Elastic-decohesive constitutive model for sea ice, *Journal of Geophysical Research-Oceans*, *111*(C11), doi:10.1029/2005JC003334.

Schulson, E. (2001), Brittle failure of ice, *Engineering Fracture Mechanics*, *68*(17-18), 1839–1887, doi:10.1016/S0013-7944(01)00037-6.

Schulson, E. (2004), Compressive shear faults within arctic sea ice: Fracture on scales large and small, *Journal of Geophysical Research*, *109*(C7), C07,016, doi:10.1029/2003JC002108.

Schulson, E., A. Fortt, D. Iliescu, and C. Renshaw (2006), On the role of frictional sliding in the compressive fracture of ice and granite: Terminal vs. post-terminal failure, *Acta Materialia*, *54*(15), 3923–3932, doi:10.1016/j.actamat.2006.04.024.

Taylor, P., D. Feltham, P. Sammonds, and D. Hatton (2006), Continuum sea ice rheology determined from subcontinuum mechanics, *J. Geophys. Res*, *111*, doi:10.1029/2005JC002996.

Thorndike, A., D. Rothrock, G. Maykut, and R. Colony (1975), The thickness distribution of sea ice, *Journal of Geophysical Research-Oceans*, *80*(33), 4501–4513.

Ukita, J., and R. Moritz (1994), Yield curves and flow rules of pack ice, *Journal of Geophysical Research-Oceans*, *100*(C3), 4545–4557.

Ukita, J., and R. Moritz (2000), Geometry and the deformation of pack ice: Ii. simulation with a random isotropic model and implication in sea-ice rheology, *Annals of Glaciology*, *31*(1), 323–326.

Weiss, J., and E. Schulson (2009), Coulombic faulting from the grain scale to the geophysical scale: lessons from ice, *Journal of Physics D: Applied Physics*, *42*(21), 214,017–.

Weiss, J., E. Schulson, and H. Stern (2007), Sea ice rheology from in-situ, satellite and laboratory observations: Fracture and friction, *Earth and Planetary Science Letters*, *255*(1-2), 1–8.

Wettlaufer, J. S. (1991), Heat flux at the ice-ocean interface, *J. Geophys. Res.*, *96*(C4), 7215–7236.

Wilchinsky, A., and D. Feltham (2004a), A continuum anisotropic model of sea-ice dynamics, *Proceedings: Mathematical, Physical and Engineering Sciences*, *460*(2047), 2105–2140, doi:http://www.jstor.org/stable/4143068.

Wilchinsky, A., and D. Feltham (2004b), Dependence of sea ice yield-curve shape on ice thickness, *Journal of Physical Oceanography*, *34*(12), 2852–2856.

Wilchinsky, A., and D. Feltham (2006a), Modelling the rheology of sea ice as a collection of diamond-shaped floes, *Journal of Non-Newtonian Fluid Mechanics*, *138*(1), 22–32, doi:10.1016/j.jnnfm.2006.05.001.

Wilchinsky, A., and D. Feltham (2006b), Anisotropic model for granulated sea ice dynamics, *Journal of the Mechanics and Physics of Solids*, *54*(6), 1147–1185, doi:10.1016/j.jmps.2005.12.006.

Wilchinsky, A., D. Feltham, and P. Miller (2006), A multithickness sea ice model accounting for sliding friction, *Journal of Physical Oceanography*, *36*(9), 1719–1738, doi:10.1175/JPO2937.1.

Wilchinsky, A., D. Feltham, and M. Hopkins (2011), Modelling the reorientation of sea-ice faults as the wind changes direction, *Annals of Glaciology*, *52*, 57–83.

Wilchinsky, A. V., and D. L. Feltham (2011), Modeling coulombic failure of sea ice with leads, *J. Geophys. Res.*, *116*(C8), C08,040–.

Wilchinsky, A. V., and D. L. Feltham (2012), Rheology of discrete failure regimes of anisotropic sea ice, *J. Phys. Oceanogr.*, pp. –.

Wilchinsky, A. V., D. L. Feltham, and M. A. Hopkins (2010), Effect of shear rupture on aggregate scale formation in sea ice, *J. Geophys. Res.*, *115*(C10), C10,002–.

Zhang, J., and D. A. Rothrock (2005), Effect of sea ice rheology in numerical investigations of climate, *J. Geophys. Res.*, *110*(C8), C08,014–.